

Mechanisms for the Generation of Mesoscale Vortices within Quasi-Linear Convective Systems

MORRIS L. WEISMAN AND CHRISTOPHER A. DAVIS

National Center for Atmospheric Research, Boulder, Colorado*

(Manuscript received 7 May 1997, in final form 14 January 1998)

ABSTRACT

Previous idealized simulations of convective systems have demonstrated that the development of mesoscale vortices within quasi-linear convective systems may be a natural consequence of the finite extent of the convective line, as horizontal vorticity is tilted into the vertical at the line ends. However, the source of this horizontal vorticity has not yet been clearly established, either being associated with the ambient shear or else generated within the system. In this paper, results are presented from a series of idealized simulations that demonstrate that the source, strength, and scale of these vortices depends on the strength of the ambient vertical wind shear, the strength of the system-generated cold pool, the scale of the convective line segments, as well as the phase within the life cycle of the convective system. In particular, for systems that develop in an environment with weak-to-moderate shear, a line-end vortex pair is generated primarily via the tilting of horizontal vorticity generated within the system-scale cold pool, as the associated vortex lines are lifted within the laterally finite front-to-rear ascending current. Similar mechanisms also operate in environments with stronger or deeper shear, but subsystem-scale vortices can also originate via the tilting of the ambient horizontal vorticity within supercell updraft–downdraft couplets. In all cases, convergence at midlevels enhances Coriolis rotation over the longer term, leading to the preferred development of a cyclonic vortex, as is frequently observed in asymmetric convective systems.

1. Introduction

Observations reveal that a variety of mesoscale convective vortices (MCVs) with horizontal scales ranging from tens to hundreds of kilometers and timescales ranging from hours to days can be generated within mesoscale convective systems (MCSs). These MCVs play a variety of roles, from locally enhancing the strength of rear-inflow jets, which may contribute to the production of damaging surface winds, to initiating the development of long-lived, balanced midtropospheric circulations, which can help trigger new convective episodes on subsequent days. Recent idealized nonhydrostatic numerical simulations demonstrate that such vortices may form as a result of the tilting of either environmental or system-generated horizontal vorticity at the ends of finite-length convective lines (Weisman 1993; Davis and Weisman 1994; Skamarock et al. 1994a). In this paper, we extend these previous studies by determining the relative importance of these two tilting mechanisms in

the formation of such vortices over a wide range of environmental vertical wind shears, and demonstrating how the strength and scales of such vortices depends on both the strength of the vertical wind shear as well as the influence of the Coriolis force.

The generation of significant convectively produced vortices on the mesoscale was first highlighted by Fujita (1978) in his description of severe bow echoes (which are especially known for producing long swaths of damaging surface winds). Such systems characteristically appear as 20- to 120-km long bow-shaped convective segments, with cyclonic and anticyclonic rotation of the rain cells often observed at the northern and southern ends of the convective system, respectively (e.g., for a system developing in a westerly sheared environment in the Northern Hemisphere). Over time, the northern cyclonic vortex becomes more dominant, eventually producing a comma-shaped convective system. Bow echoes are observed both as isolated features or as a sequence of smaller-scale bow-shaped convective segments within a larger-scale squall line, suggesting a range of possible scales for the associated mesoscale vortices (e.g., Johns and Hirt 1987; Schmidt and Cotton 1989; Burgess and Smull 1990; Przybylinski 1995).

More recent observational studies have emphasized the generation of mesoscale vortices on even larger scales (e.g., hundreds of kilometers), for instance, in association with squall lines or other types of MCSs

* The National Center for Atmospheric Research is sponsored by the National Science Foundation.

Corresponding author address: Dr. Morris L. Weisman, NCAR/MMM, P.O. Box 3000, Boulder, CO 80307–3000.
E-mail: weisman@ncar.ucar.edu

(e.g., Maddox 1980; Menard and Fritsch 1989; Stirling and Wakimoto 1989; Brandes 1990; Bartels and Maddox 1991; Smull and Augustine 1993; Fritsch et al. 1994). The preponderance of these mesoscale vortices has led to a reevaluation of the paradigm of quasi-two-dimensional (quasi-linear) convective systems, and it is now generally recognized that two general conceptual models exist for such systems (e.g., Houze et al. 1989; Houze et al. 1990). The first, referred to as a symmetric MCS, essentially represents the old two-dimensional squall-line model, including the usual front-to-rear ascending and rear-to-front descending airflow currents. Nearly equal-strength cyclonic and anticyclonic midlevel vortices are sometimes observed behind the northern and southern ends of the convective system, respectively. The second, referred to as an asymmetric convective system, includes a dominant cyclonic vortex along with an enhanced stratiform precipitation region on the northern end of the system in addition to the quasi-two-dimensional airstreams described above. Furthermore, rather than representing two distinct types of MCSs, observational evidence is mounting that symmetric and asymmetric structures represent stages in the evolution of such convective systems, with the symmetric structure characteristic of the early phase of evolution and the asymmetric structure characteristic of the later phases (e.g., Scott and Rutledge 1995; Loehrer and Johnson 1995). While the above studies have only considered midlatitude convective systems, Jorgensen et al. (1997) similarly document the development of mesoscale vortices in association with a tropical convective system observed during TOGA COARE.

From the above observations, it is clear that MCVs are generally quite distinct from the mesocyclones and mesoanticyclones associated with supercell storms (e.g., Klemp 1987), the latter generally occurring on scales less than 10 km, and being directly associated with intense cellular-scale updrafts and downdrafts. Instead, the circulations associated with the mesoscale vortices often encompass several convective cells, suggesting that a system-scale process is responsible for their formation. Furthermore, while supercell-related vortices are restricted primarily to strongly sheared environments, mesoscale vortices are observed in both weak- and strong-shear environments.

Similar to the observations, idealized modeling studies have also demonstrated that a variety of mesoscale vortices may be generated within long-lived convective systems. Weisman (1993) found that under conditions of strong low-level vertical wind shear and large CAPE, small, long-lived bow-shaped segments of convective cells were likely to form, similar to the systems described by Fujita (1978). These simulated systems were characterized by a strong, central rear-inflow jet, with 10- to 30-km wide cyclonic and anticyclonic midlevel vortices (referred to as “book-end vortices”) found just behind the northern and southern ends of the system (for westerly shear), respectively. Without Coriolis forc-

ing, the book-end vortices were of equal strength, but in simulations that included Coriolis forcing, the cyclonic vortex eventually became stronger than the anticyclonic vortex (e.g., after 4 h; Weisman 1993). At early times (i.e., 2–3 h), the source of the vertical vorticity could be traced to the upward- and subsequent downward-tilting of ambient horizontal vorticity at the ends of the convective segments. Analyses for later times (i.e., 3–4 h), however, suggested an additional source of vertical vorticity that was not clearly identified.

Skamarock et al. (1994a) demonstrated more generally that mesoscale vortex formation was a natural component of the evolution of any finite extent convective line, even in the presence of relatively weak vertical wind shear. Starting with a 200-km long line of convective cells in a weak, westerly sheared environment (10 m s^{-1} wind variation over the lowest 2.5 km AGL), cyclonic and anticyclonic vortices formed behind the northern and southern ends of the line after 3 h. With the Coriolis force included, the cyclonic vortex eventually dominated (after 4 h), producing a system structure and evolution that resembled observed asymmetric convective systems, as described by Houze et al. (1990), etc. The size of the vortices in the Skamarock study was 40–60 km, with the vortices found well to the rear of the active leading-line convection, within the stratiform precipitation region. The development of the asymmetric structure was clearly linked to the system-scale midlevel convergence of Coriolis rotation, which enhanced the cyclonic line-end vortex and weakened the anticyclonic line-end vortex. However, the origin of the original line-end vortices was not clearly established.

Davis and Weisman (1994) further analyzed the Skamarock et al. (1994a) system-scale vortices and suggested that the origin of the vortices could ultimately be traced to the upward tilting of system-generated horizontal vorticity by the leading line convective updrafts. The primary source for this horizontal vorticity was the cold-pool-updraft interface, with the sign of the horizontal vorticity opposite that found in the ambient shear layer. The role of the ambient horizontal vorticity was relegated to promoting the preferred downshear development of the leading-line updraft, which effectively produced the finite region of active convection.

Trier and Parsons (1995) and Trier et al. (1996; 1997) produced similar mesoscale vortices in simulations of weakly sheared tropical convective systems observed during TAMEX and TOGA COARE, respectively. A detailed analysis of a dominant cyclonic line-end vortex simulated for the TOGA COARE case (Trier et al. 1997) suggested that the source of the vorticity was again tilting of horizontal vorticity generated within the system-scale cold pool, as in the midlatitude case studied by Davis and Weisman (1994).

The goal of the present study is to systematically investigate the origins of such mesoscale vortices over the wide range of shear environments for which they

are observed, to help clarify the mechanisms of formation and the factors that control their strength and scale. Through the use of idealized simulations of finite length squall lines, we will show that mesoscale vortices are produced behind the ends of the convective line for the entire range of shears considered. In addition, we will show that there is an increasing tendency to produce smaller pairs of vortices located at the ends of bow-shaped convective segments within the line for increasing strength and depth of the ambient shear. For all scales and environmental shears, these line-end vortices are forced primarily by the localized lifting (tilting) of the horizontal vorticity generated within the system, associated with the cold-pool-updraft interface, as hypothesized by Davis and Weisman (1994) and Trier et al. (1997). For the stronger and deeper shears, however, we will show that the smaller-scale vortices may be initiated through the tilting of the ambient shear within supercellular updraft-downdraft couplets at the ends of convective line segments, as hypothesized by Weisman (1993). In all cases, the role of the Coriolis force is to gradually promote the development of the northern, cyclonic line-end vortex (over a 4- to 6-h time period), producing the more commonly observed asymmetric structures.

We will begin in section 2 with a description of the experimental methodology, followed in section 3 by a general description of the various simulations. In section 4, we will present a detailed analysis of the vortex-line structure for the various simulations, which helps to clarify the source for the vertical vorticity in each case. We will continue this discussion in section 5 with an analysis using the flux form of the vertical-vorticity equation, which is especially useful in highlighting the role of the line ends in vortex formation, followed in section 6 by a discussion of Coriolis influences. We will finish in section 7 with a summary discussion and goals for future research.

2. Experimental design

Simulations are conducted using the Klemp-Wilhelmson (1978) model in a domain of uniform 2-km horizontal grid length, 600 km on a side. The vertical grid length is 700 m. The environment is initialized with a horizontally uniform thermodynamic profile used by Skamarock et al. (1994a), which contains about 2400 J kg^{-1} of convective available potential energy (CAPE) (Fig. 1). Convection is also initiated as in Skamarock et al. (1994a), with the exception that a line of five uniformly spaced, warm (maximum 2 K) bubbles 160 km in length is used rather than a line of six bubbles 200 km in length. This slightly smaller initial line length has the effect of accelerating the evolution of system-scale features somewhat, but otherwise does not effect the conclusions. In general, we have found that the features we are describing are independent of these aspects of the initial convective triggering.

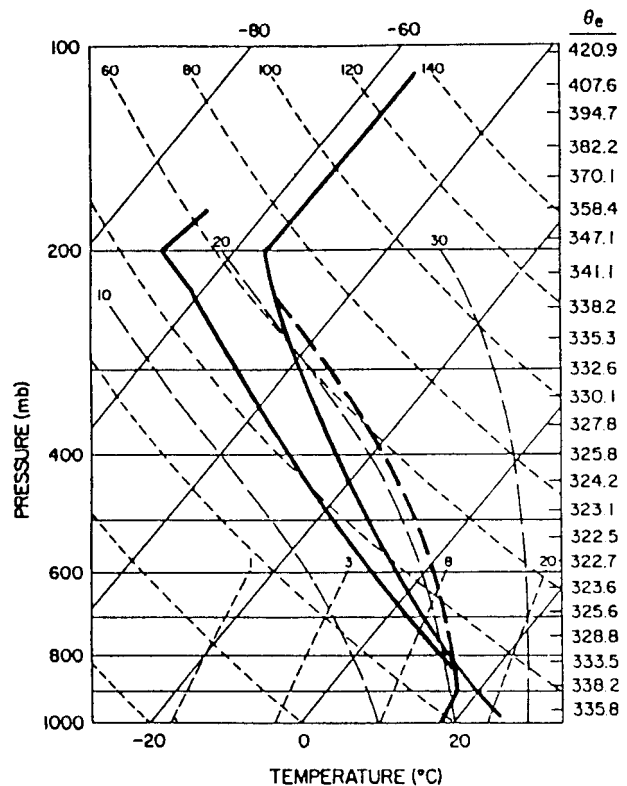


FIG. 1. Initial temperature and moisture sounding used in model simulations.

Ice processes are not included in the present simulations in order to help simplify the interpretation of the results. As discussed by Skamarock et al. (1994b), the inclusion of ice microphysics has the effect of increasing the size and accelerating the evolution of the circulation within the stratiform precipitation region somewhat, but otherwise does not significantly affect the basic mechanisms of vortex formation and evolution.

Simulations are presented for two low-level westerly shear environments, representing a linear increase in wind speed of either $U_s = 10 \text{ m s}^{-1}$ or 20 m s^{-1} between the ground and 2.5 km AGL, with constant winds above, and for a deeper westerly shear environment, with an increase of $U_s = 30 \text{ m s}^{-1}$ extending over the lowest 5 km AGL (Fig. 2). The $U_s = 10 \text{ m s}^{-1}$ case represents a weak-shear scenario for which the initial strong line of convective cells quickly evolves to a weaker, upshear-tilted configuration over the initial 3–4 h. The $U_s = 20 \text{ m s}^{-1}$ case represents a moderate-to-strong shallow shear case for which the system maintains a stronger, more upright leading convective line throughout the 6 h. Finally, the $U_s = 30 \text{ m s}^{-1}$ deeper-shear case also maintains strong leading-line convection throughout the 6 h, with the addition of supercellular structures within the line.

Each simulation is run for 6 h, both with and without Coriolis effects included. Since the most critical period

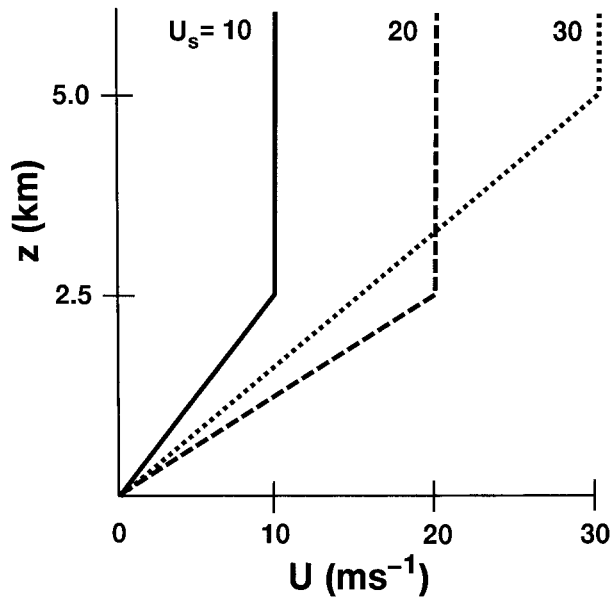


FIG. 2. Wind profiles used in model simulations.

of vortex formation in these simulations is the initial 3–4 h, over which time period Coriolis effects are relatively minimal (Skamarock et al. 1994a), our focus will be on the analysis of the non-Coriolis simulations, for which the mechanisms of vortex formation are most easily revealed. For the Coriolis runs, technically, a thermal wind balance should be included as part of the base state, with the westerly shear balanced by an appropriate north–south temperature gradient. The effects of thermal wind balance on the evolution of three-dimensional convective systems for weaker vertical wind shears is discussed by Skamarock et al. (1994b), where it is shown that the basic mechanisms of line-end vortex formation are not significantly impacted by the inclusion of such north–south environmental variability.

3. Simulation overviews

The results for the three shear experiments are summarized in Figs. 3 and 4, which present the rainwater mixing ratio, updraft, and approximate storm relative flow at 2 km AGL at 3, 4.5, and 6 h for the non-Coriolis and Coriolis simulations, respectively. For the $U_s = 10$ and 20 m s^{-1} shear simulations, only a 200 km by 260 km portion of the full 600 km by 600 km domain is

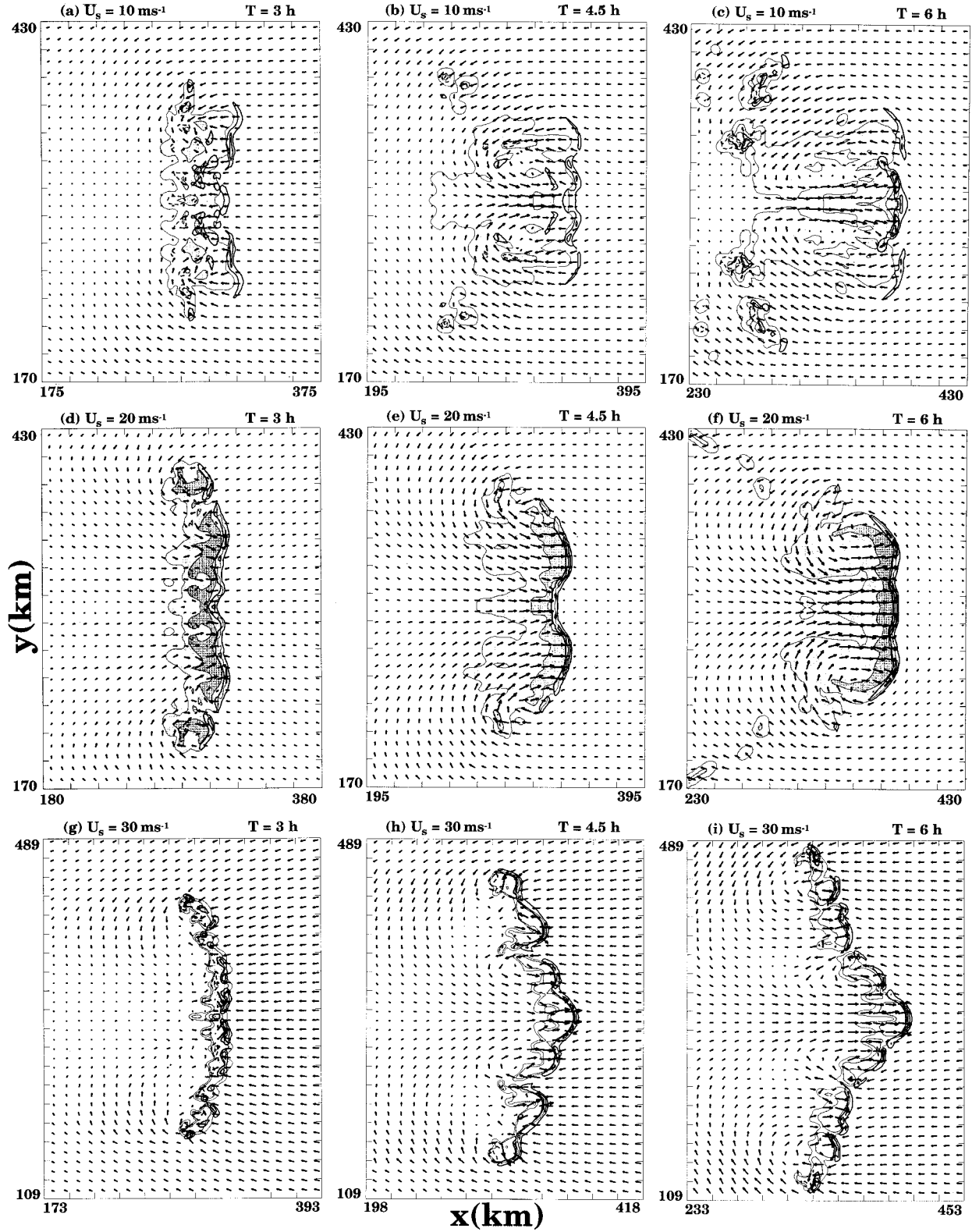
shown, but for the $U_s = 30 \text{ m s}^{-1}$ shear simulation, a 220 km by 380 km portion of the full domain is shown, due to the larger size of the resulting convective line. During the initial 3 h, the simulations all exhibit fairly classic symmetric-type squall-line structure, with a sequence of convective updrafts and downdrafts feeding an expanding and strengthening surface cold pool.

By 3 h, the leading-line convection for the $U_s = 10 \text{ m s}^{-1}$ simulations is already quite weak (Fig. 3a), with the vertical circulation exhibiting a pronounced upshear tilt consisting of a front-to-rear ascending current feeding into a broad region of mostly light precipitation (not shown). The stronger-shear cases (Figs. 3d and 3g), however, are still composed of strong, leading-line convective cells (in association with a more upright vertical circulation), consistent with a more optimal balance between the cold-pool-generated circulation and the stronger low-level vertical shear (e.g., Rotunno et al. 1988; Weisman et al. 1988; Weisman 1992). The weak-shear simulation shows some sign of developing line-end vortices at this time, but the line-end vortices are already quite evident in both of the stronger-shear cases. Although all simulations began with equal-length convective lines, the stronger, deeper-shear cases have grown significantly, with the $U_s = 20 \text{ m s}^{-1}$ case now over 200 km in length and the $U_s = 30 \text{ m s}^{-1}$ case nearly 300 km in length. We believe that this scale lengthening is a result of the more-optimal balance between the cold pool and ambient wind shear for the stronger-shear cases, more readily allowing new cells to be triggered along the expanding cold pool.

By 4.5 h, the flow field for the $U_s = 10 \text{ m s}^{-1}$ shear case (Fig. 3b) is highlighted by a rear-inflow jet at the center of the system, with 50-km mirror-image cyclonic and anticyclonic vortices within the region of light precipitation, north and south of the jet core, respectively. In comparison, the $U_s = 20 \text{ m s}^{-1}$ non-Coriolis simulation at 4.5 h (Fig. 3e) is composed of a much stronger updraft and rainfall at the leading edge, with two symmetric bow-shaped precipitation regions evident north and south of the symmetry axis. The flow field depicts a much broader rear inflow current extending right up to the leading edge of the system, with strong cyclonic and anticyclonic vortices located just behind the leading edge convection, at the northern and southern ends of the system, respectively. The $U_s = 30 \text{ m s}^{-1}$ deeper shear non-Coriolis case at 4.5 h (Fig. 3h) similarly exhibits strong leading-line convection with a broad zone

FIG. 3. Horizontal cross sections of system-relative flow, rainwater mixing ratio, and vertical velocity at 2 km AGL for the (a), (b), (c) $U_s = 10 \text{ m s}^{-1}$ 2.5-km shear, (d), (e), (f) $U_s = 20 \text{ m s}^{-1}$ 2.5-km shear, and (g), (h), (i) $U_s = 30 \text{ m s}^{-1}$ 5.0-km shear non-Coriolis simulations at 3, 4.5, and 6 h, respectively. Vectors are presented every four grid points (8 km), with a vector length of 8 km equal to a wind magnitude of 20 m s^{-1} , except for the $U_s = 30 \text{ m s}^{-1}$ case, for which vectors are presented every five grid points (10 km), with a vector length of 10 km equal to a wind magnitude of 20 m s^{-1} . The rainwater is contoured for magnitudes greater than 1 g kg^{-1} (lightly shaded) and magnitudes greater than 3 g kg^{-1} (darkly shaded). The vertical velocity is contoured at 2.5 m s^{-1} intervals for the $U_s = 10 \text{ m s}^{-1}$ case, and 5 m s^{-1} intervals for the $U_s = 20$ and 30 m s^{-1} cases, with the zero contours omitted. A domain speed of $u_m = 13.0, 18.5,$ and 18.5 m s^{-1} has been subtracted from the flow field for the $U_s = 10, 20,$ and 30 m s^{-1} shear cases, respectively. Tick marks are spaced 20 km apart.

W, Q_R Z = 2.0 km f = 0.0



W, Q_R Z = 2.0 km f = 0.0001

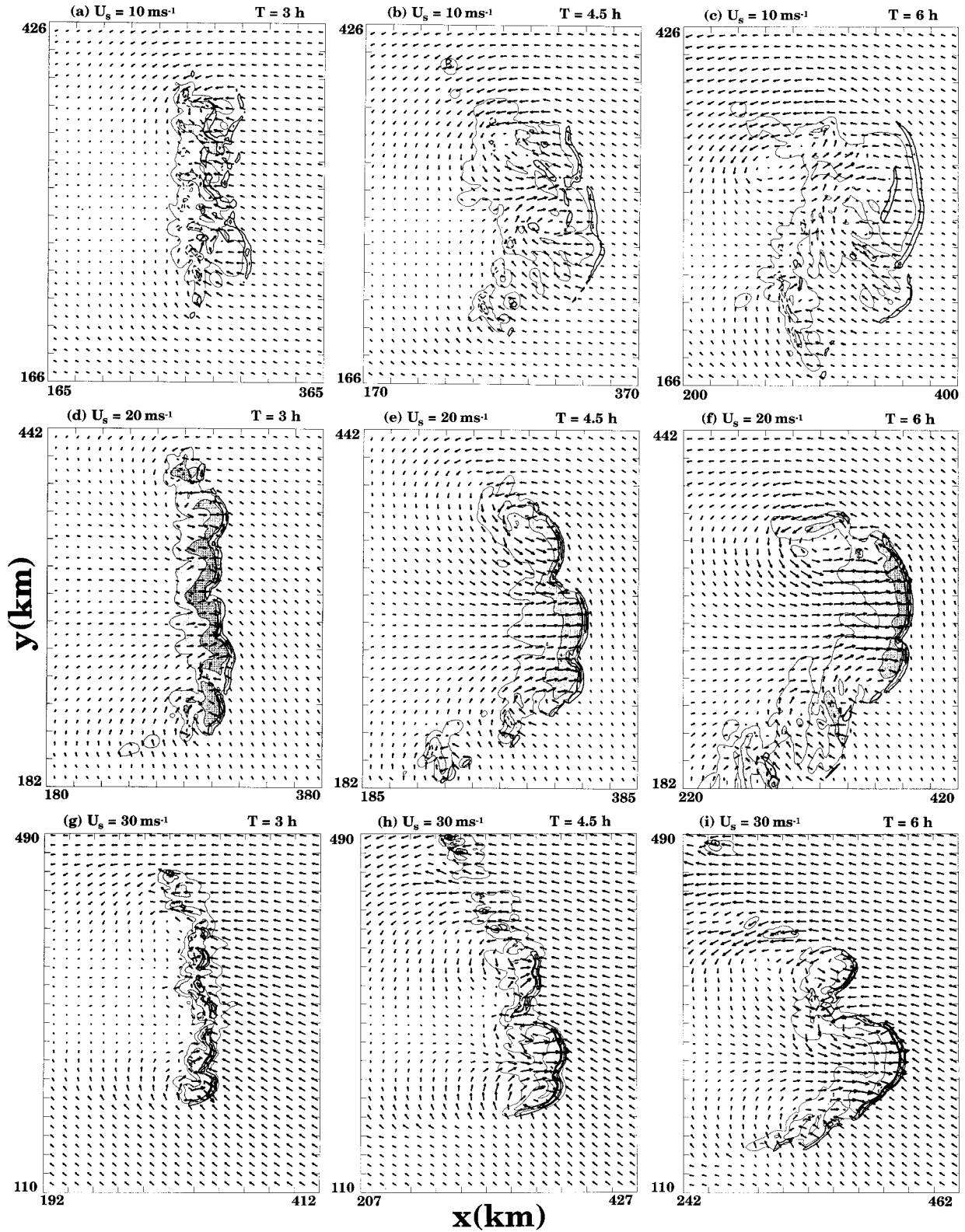


FIG. 4. Same as Fig. 3, except for the Coriolis simulations. A domain speed of $(u_m, v_m) = (13.0, -1.0), (18.5, -2.5),$ and $(19.5, -3.0) \text{ m s}^{-1}$ has been subtracted from the flow field for the $U_s = 10, 20,$ and 30 m s^{-1} shear cases, respectively.

of rear inflow extending rearward. This leading line, however, is broken up into many smaller-scale bow-shaped convective segments, each exhibiting cyclonic and anticyclonic book-end vortices at the various line-segment ends. The rear inflow is strongest behind the center of the system, which also exhibits the most bowed-out structure.

By 6 h, the cyclonic and anticyclonic vortices for the $U_s = 10 \text{ m s}^{-1}$ case have extended farther rearward of the leading-line convection, with the rear-inflow jet between the vortices having strengthened somewhat (Fig. 3c). For the $U_s = 20 \text{ m s}^{-1}$ non-Coriolis case (Fig. 3f), the two vortices have strengthened significantly and grown somewhat in size, and are still attached to the northern and southern ends of the strong leading line of convective cells. Finally, for the $U_s = 30 \text{ m s}^{-1}$ deeper-shear case at 6 h (Fig. 3i), the strong, leading line of convective cells has continued to grow in extent, still being composed of many smaller bow-shaped convective segments and associated line-end vortices. However, the strongest bow-shaped segment and associated rear-inflow jet is still found at the center of the system.

A comparison of the Coriolis and non-Coriolis simulations for the three shear cases at 3 h (Figs. 3a,d,g and 4a,d,g) reveals minimal differences, as would be expected based on scaling arguments. However, by 4.5 h (Figs. 4b,e,h), the mirror-image symmetry of the non-Coriolis simulations is broken, with the cyclonic vortices beginning to dominate on the northern end of the system, especially for the $U_s = 10$ and 20 m s^{-1} cases. For the $U_s = 20 \text{ m s}^{-1}$ Coriolis case (Fig. 4f), two bow-shaped convective segments are now also evident along the line, with smaller, strong cyclonic and anticyclonic vortices located at the ends of the respective convective line segments. For the $U_s = 30 \text{ m s}^{-1}$ Coriolis simulation at 4.5 h (Fig. 4h), the system is composed of a primary bow-shaped system at the southern end of the line, with smaller bow-shaped segments extending northward. The cyclonic line-end vortices are only a bit more dominant than the anticyclonic vortices at this time.

By 6 h, the cyclonic vortex for the $U_s = 10 \text{ m s}^{-1}$ Coriolis simulation has continued to become more dominant and is now found at the back edge of the region of light precipitation (Fig. 4c). For the $U_s = 20 \text{ m s}^{-1}$ Coriolis case, the two bow-shaped convective segments at 4.5 h have congealed into one primary strong bow-shaped convective segment by 6 h, with a dominant cyclonic vortex at its northern end (Fig. 4f). Finally, for the $U_s = 30 \text{ m s}^{-1}$ Coriolis simulation, the dominant bow-shaped segment at the southern end of the system at 4.5 h has become even more dominant by 6 h, with the cyclonic vortex on its northern end now much stronger than the anticyclonic vortex to the south (Fig. 4i). The smaller bow-shaped segment to the north of the southern bow at 4.5 h has also maintained its coherence through 6 h, also now exhibiting a more dominant cyclonic vortex on its northern side.

In summary, significant mesoscale vortices are gen-

erated in all three shear simulations after 3 h. For the weakest shear case, a single pair of vortices is generated that extends significantly behind the northern and southern ends of the main zone of active convection. A similar pattern is produced in the stronger and deeper shear cases, with the exception that the pair of vortices is closer to the leading edge of the system. There is also an increasing tendency to produce smaller-scale pairs of vortices along the line for stronger and deeper shears, in association with smaller bow-shaped convective segments. For the purposes of the following discussions, we will refer to the primary pair of vortices associated with the system-scale line ends as system-scale vortices. The smaller-scale pairs of vortices associated with the ends of convective segments within the line will be referred to as subsystem-scale vortices. For all three shear cases, the influence of Coriolis forcing promotes the development of the northern cyclonic vortices at the expense of the southern anticyclonic vortices, leading to asymmetric convective structures either on the system or subsystem scale.

4. Mechanisms of vortex development: Vortex line diagnostics

The primary goal of this paper is to trace the source of both the system-scale and subsystem-scale mesoscale vortices produced in the above simulations. This analysis will be guided by the three-dimensional vorticity equation for inviscid, Boussinesq motion with a constant Coriolis parameter,

$$\frac{d\boldsymbol{\omega}}{dt} = (\boldsymbol{\omega} + f\mathbf{k}) \cdot \nabla \mathbf{v} + \nabla \times (B\mathbf{k}), \quad (1)$$

where $\boldsymbol{\omega}$ is the vorticity vector, \mathbf{v} is the velocity vector, \mathbf{k} is the vertical unit vector, f is the Coriolis parameter, and B represents the buoyancy field, given by

$$B \equiv g \left[\frac{\theta'}{\bar{\theta}} + 0.61(q_v - \bar{q}_v) - q_c - q_r \right], \quad (2)$$

where $\bar{\theta}$ is the mean potential temperature, θ' is the perturbation potential temperature, and q_v , q_c , and q_r are the mixing ratios of water vapor, cloud water, and rainwater, respectively. The first term on the right of (1) represents the effects of tilting and stretching, which alters an existing vorticity field, while the second term represents the generation of horizontal components of vorticity by horizontal gradients of buoyancy. In describing the evolution of the line-end vortices, we will be especially interested in the vertical component of the vorticity equation, which is given by

$$\frac{d\zeta}{dt} = \boldsymbol{\omega}_H \cdot \nabla_H w + (\zeta + f) \frac{\partial w}{\partial z}, \quad (3)$$

where $\boldsymbol{\omega}_H$ represents the horizontal components of the vorticity vector ($\partial w / \partial y - \partial v / \partial z$, $\partial u / \partial z - \partial w / \partial x$), $\zeta = \partial v / \partial x - \partial u / \partial y$ is the vertical component of vorticity, w

is the vertical velocity, and the first and second terms on the right represent the usual tilting and stretching effects, respectively. In an initially horizontally homogeneous, nonrotating, Boussinesq fluid, vertical vorticity may only be generated by tilting the horizontal vorticity, ω_H , inherent in the ambient flow. Once convection begins, however, horizontal gradients of buoyancy will generate additional horizontal vorticity that can also be tilted into the vertical. Coriolis influences are included in the vertical stretching term.

In tracing the source of the line-end vortices, it will be helpful to visualize the system-scale vorticity structure through the use of vortex lines, which are especially useful for highlighting the process of vortex tilting as the vortex lines are deformed by the evolving flow field. In particular, we are looking for a pattern of vortex-line evolution that systematically produces a cyclonic vortex at the northern end of the line and anticyclonic vorticity at the southern end of the line. Since there is no vertical vorticity initially for the present non-Coriolis simulations, the only possible source of the line-end vertical vorticity is the tilting of either ambient or system-generated horizontal vorticity. As depicted schematically in Fig. 5, there are two possible ways in which initially horizontal vortex lines can be deformed to produce the observed pattern of line-end vorticity; either a localized downdraft in westerly shear (Fig. 5a) or a localized updraft in easterly shear (Fig. 5b). For the present simulations, the environment is characterized by westerly shear alone, with easterly shear found primarily at the cold-pool-updraft interface, such shear having been generated by the convective system itself. For strongly sheared environments, Weisman (1993) concluded that it was downdrafts in the ambient westerly shear that lead to the early development of the book-end vortices for strongly sheared bow-echo simulations, although the source of the vertical vorticity for the later intensification of these features was not clearly discerned. However, for weaker-shear simulations, both Davis and Weisman (1994) and Trier et al. (1997) hypothesized that it was upward tilting of the horizontal vorticity associated with easterly shear, which was generated primarily by the system-scale cold pool, that was the dominant source of vertical vorticity for their line-end vortices.

We will begin this discussion with a more complete description of the three-dimensional vorticity field for the three simulations. In this portion of the analysis, we will only consider the non-Coriolis simulations, since the basic vortex formation mechanisms do not appear to depend on Coriolis influences.

a. The $U_s = 10 \text{ m s}^{-1}$ shallow-shear simulation

In the previous section, we established that the line-end vortices for the $U_s = 10 \text{ m s}^{-1}$ shallow-shear simulations were generated primarily between 3 and 4.5 h. The line-end vortex structure at 2 km AGL for the non-

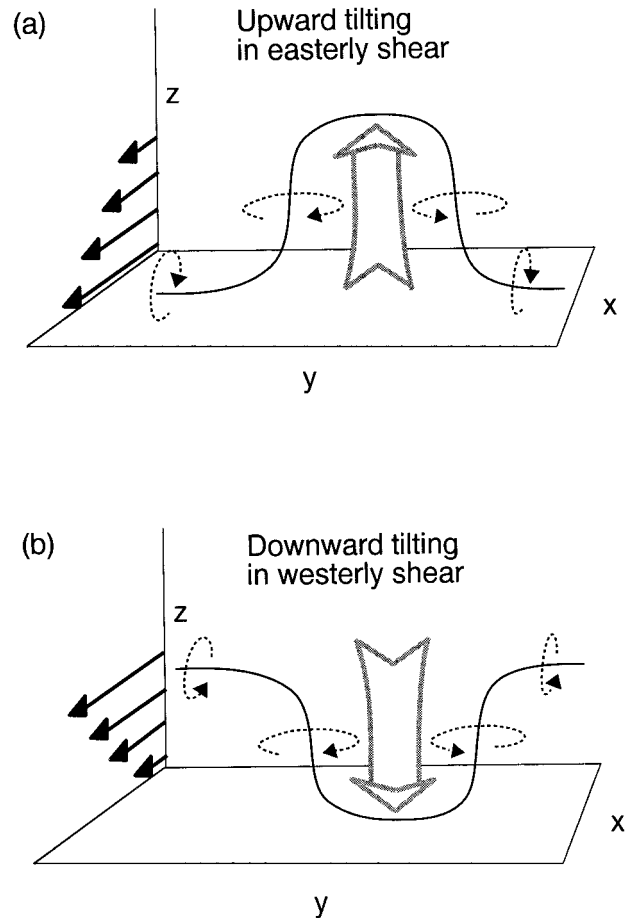


FIG. 5. Schematic of vertical vorticity generation through vortex tilting. For westerly shear (a), descending motion pushes the vortex lines down in the center, resulting in cyclonic rotation on the north end and anticyclonic rotation on the south end. Localized ascent in easterly shear (b) produces the same vertical vorticity pattern.

Coriolis simulation is depicted at 4 h in Fig. 6, overlaid with a shaded field of θ_e at the same level. Due to the simulation's mirror-image symmetry, only the southern half of the system is presented. The location of the vortices on the gradient between high and low θ_e is consistent with the approximate conservation of equivalent potential vorticity, as discussed by Rotunno and Klemp (1985). Since there is zero equivalent potential vorticity to begin with, vortex lines are constrained to remain on the θ_e surfaces upon which they originate (assuming no mixing), and will be deformed identically as the θ_e surfaces are deformed by updrafts and downdrafts. This results in vortex lines tilting vertically through zones of horizontal gradients of θ_e , consistent with the observed vertical vorticity pattern. Trajectory analyses (not shown) demonstrate that air feeding the southern high- θ_e region of the vortex at this height originates in the 1–2 km AGL level in the ambient air mass ahead of the system, while air feeding the northern, low- θ_e portion

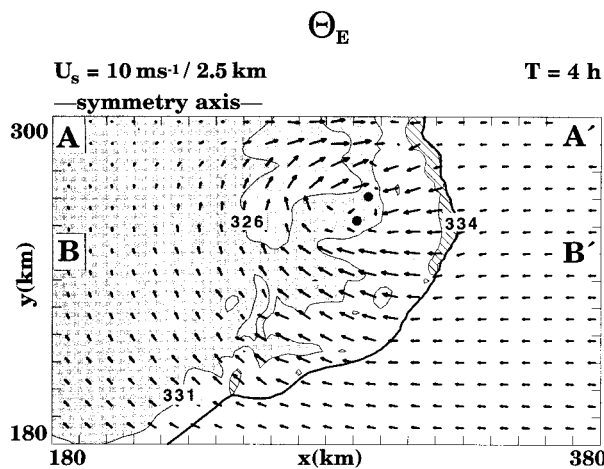


FIG. 6. Horizontal cross section of system-relative flow and θ_e at 2 km AGL for the $U_s = 10 \text{ m s}^{-1}$ simulation at 4 h. Flow vectors are presented every four grid points (8 km), with a vector length of 8 km equal to a wind magnitude of 20 m s^{-1} . The field of θ_e is contoured for values greater than 334 K (lightly cross hatched), 331 to 334 K (clear), 326 to 331 K (darkly shaded), and 320 to 326 K (lightly shaded). The solid line depicts the location of the cold-pool boundary at the surface (-1 K contour). A domain speed of $u_m = 13.0 \text{ m s}^{-1}$ has been subtracted from the flow field. Dots represent the location in this cross section of the vortex lines presented in Fig. 9. Tick marks are spaced every 10 km. Only the southern half of the north-south symmetric domain is presented.

of the vortex originates to the rear of the system, having descended from 3–4 km AGL.

The vertical structure of the system at 4 h is presented in Figs. 7a,b, which depicts east-west vertical cross sections of the system-relative flow and horizontal vorticity (shaded) along both the symmetry axis and just south of the vortex, respectively, as located on Fig. 6. Along the symmetry axis, the flow is characterized by a gradually sloped front-to-rear ascending current, with a rear-inflow jet beneath that descends and spreads along the surface about 30 km behind the leading edge of the system. The horizontal vorticity field is dominated by a strip of negative horizontal vorticity that extends from just behind the leading edge of the system at the surface, and slopes upward and rearward, between the ascending front-to-rear and descending rear-inflow jets. Since the ambient horizontal vorticity is weakly positive, this negative vorticity must all be generated within the system, both by the horizontal buoyancy gradients at the leading edge of the surface cold pool as well as within the horizontal buoyancy gradients that extend rearward within the anvil outflow aloft (Fig. 8). Advection within the front-to-rear and rear-inflow currents then spreads the horizontal vorticity more continuously from these source regions.

The vertical cross section to the south of the line-end vortex (Fig. 7b) depicts a much shallower circulation, with the ambient flow simply being lifted and accelerated rearward over the cold pool, which is characterized by the shallow region of strong negative horizontal

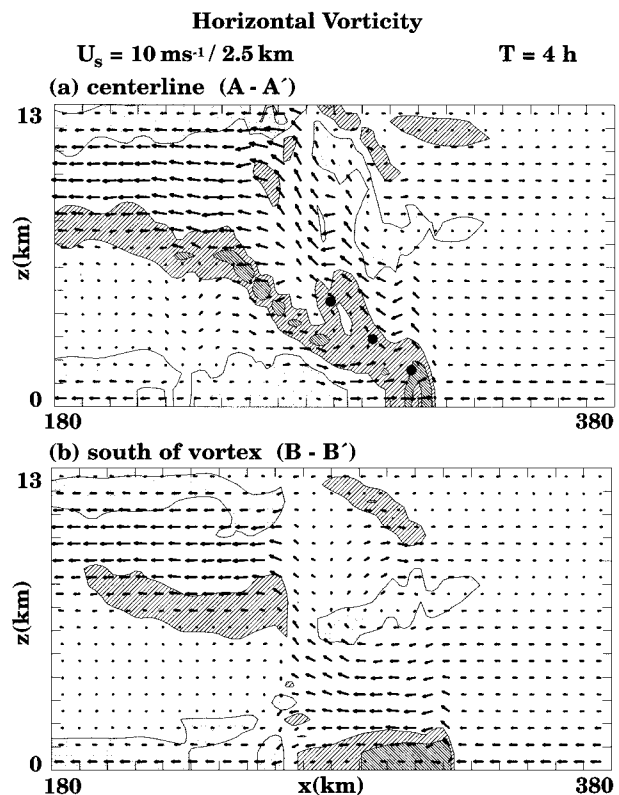


FIG. 7. East-west vertical cross sections of system-relative flow and horizontal vorticity for the $U_s = 10 \text{ m s}^{-1}$ simulations at 4 h, located (a) through the centerline of the system (A-A'), and (b) south of the line-end vortex (B-B'), as located on Fig. 6. Vectors are presented every three grid points in the horizontal (6 km), and every grid point in the vertical, with a horizontal vector length of 6 km equal to a wind magnitude of 22.5 m s^{-1} . Horizontal vorticity is contoured for magnitudes greater than $150 \times 10^{-4} \text{ s}^{-1}$ (darkly shaded), 50 to 150 (lightly shaded), -50 to -150 (lightly cross hatched), and -150 to -450 (darkly cross hatched). A domain speed of $u_m = 13.0$ has been subtracted from the flow field. Dots represent the location in this cross section of the vortex lines presented in Fig. 9. Tick marks are located every 10 km in the horizontal and every 1 km in the vertical.

vorticity. Rear-to-front flow is found only in a shallow layer near the surface just behind the leading edge of the cold pool.

A series of vortex lines emanating from the line-end vortex at 2 km in Fig. 6 are displayed in Fig. 9 to help clarify the three-dimensional characteristics of the vorticity field. For the purpose of constructing the vortex lines, the vorticity field has been smoothed using a five-gridpoint running mean filter in the horizontal, to help highlight more of the system-scale rather than cellular-scale features. Both the northern and southern sides of the symmetric system are included in this figure for completeness. The locations of the vortex lines as they cut through the cross sections in Figs. 6 and 7a are indicated by large dots in those figures. A vortex-line characteristic of the ambient low-level westerly shear ahead of the system is also depicted. The series of vortex lines that pass through the line-end vortices originate at

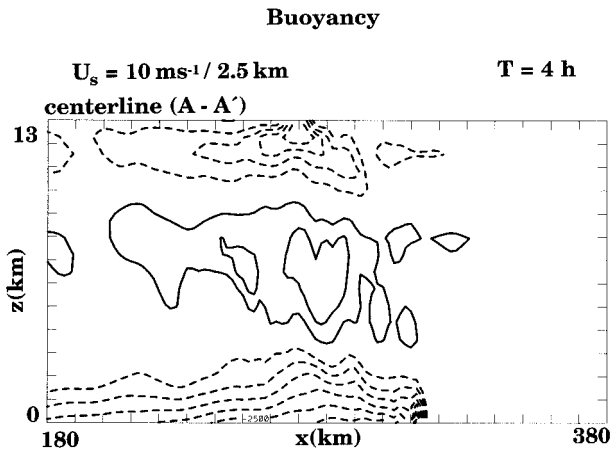


FIG. 8. East-west vertical cross section of buoyancy for the $U_s = 10 \text{ m s}^{-1}$ simulations at 4 h, located through the centerline of the system (A-A'), as located on Fig. 6. The buoyancy field is contoured using a $500 \times 10^{-4} \text{ m s}^{-2}$ interval, with the zero contour omitted. Tick marks are located every 10 km in the horizontal and every 1 km in the vertical.

lower levels within the cold pool, both north and south of the vortices, and tilt upward and then back downward through the vortices through the northern and southern ends of the system, respectively. The arc traced out by this vortex-line pattern is shallowest near the leading edge of the system, becoming substantially deeper toward the rear of the system. The vorticity vector points from north to south along the lines, consistent with negative horizontal vorticity along the horizontal portions of the lines. The ambient vortex line, however, points toward the north, consistent with the positive horizontal vorticity associated with the low-level ambient westerly shear.

We can trace the origin of the air parcels making up these vortex lines by following parcel trajectories backward in time, originating along the vortex lines. For this purpose, trajectories are approximated using model winds saved at 5-min intervals, with the trajectories followed backward for 100 min. In calculating the trajectories, it is assumed that no mixing occurs along the parcel paths. To validate this assumption, the presented trajectories have been submitted to much sensitivity testing, and we are confident that they properly represent the primary source regions for the parcels making up the vortex lines.

These trajectories (Fig. 10) are shown for the westernmost vortex line in Fig. 9, and demonstrate that the air parcels that compose this vortex line originate both from the potentially warm low levels ahead of the system as well as from the potentially cold midlevels from the rear of the system. These cold air parcels first descend within the rear-inflow jet before ascending upward to the level of the vortex line. This analysis is consistent with the vortex lines originating in the horizontal buoyancy gradient zone located between the updraft and downdraft. Since the strongest horizontal buoyancy gradients and associated negative horizontal vorticity are located near

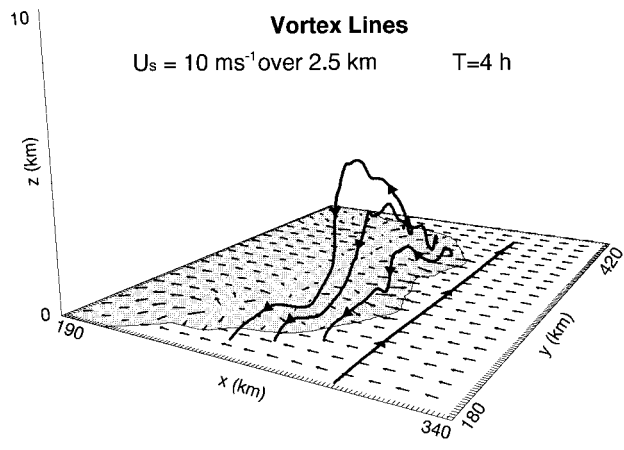


FIG. 9. Vortex-line structure at 4 h for the $U_s = 10 \text{ m s}^{-1}$ non-Coriolis simulation. The vortex lines are denoted by the thick solid lines, with the direction of the vorticity vector indicated by the arrow heads. Vectors denote the surface wind flow, and are included every 12 km, with a vector length of 12 km equal to a wind magnitude of 30 m s^{-1} . The surface cold pool (less than -1 K) is shaded. Only a 200 km by 240 km by 10 km portion of the full domain is shown.

the leading edge of the surface cold pool, one can envision horizontal vortex lines being generated primarily within this zone and being advected rearward within the front-to-rear ascending current. Since the extent of this front-to-rear ascending current is finite in the north-south direction, the vortex lines must extend downward at the northern and southern ends, producing the observed line-end vortex pattern. This scenario for line-end vortex formation is thus most consistent with that described schematically in Fig. 5b, for the localized lifting of vortex lines within an easterly shear.

This basic pattern is maintained through the remainder of the simulation, with the line-end vortices becoming even larger in extent, and extending even farther rearward of the leading edge of the system (e.g., Figs. 3b,c).

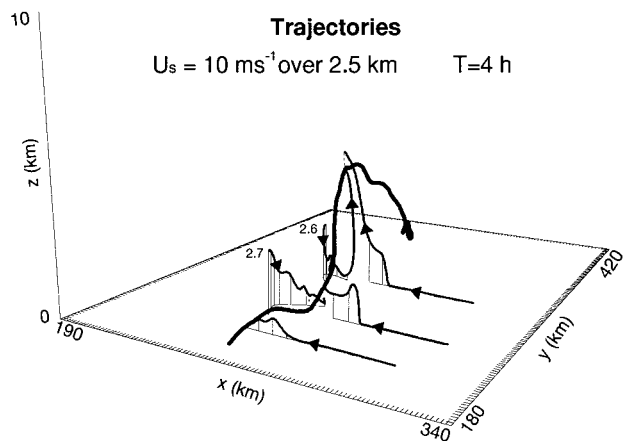


FIG. 10. Vortex-line and associated time-dependent trajectories at 4 h for the $U_s = 10 \text{ m s}^{-1}$ non-Coriolis simulation. The vortex line is denoted by the thick solid line. Trajectories are denoted by thinner solid lines, with the direction of the flow indicated by the arrow heads.

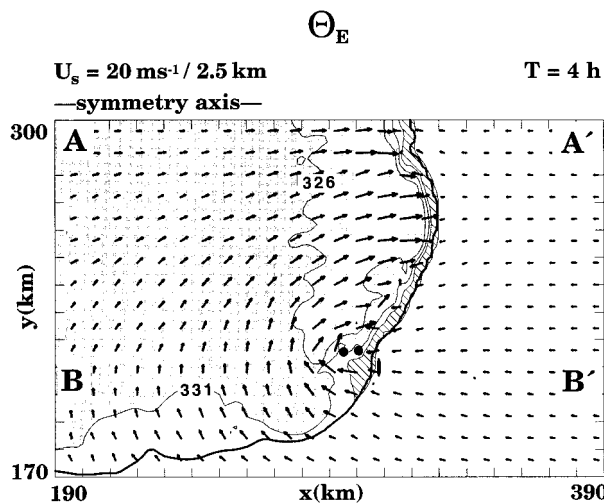


FIG. 11. Horizontal cross section of system-relative flow and θ_e at 2 km AGL for the $U_s = 20 \text{ m s}^{-1}$ simulation at 4 h, as described in Fig. 6. A domain speed of $u_m = 18.5 \text{ m s}^{-1}$ has been subtracted from the flow field.

b. The $U_s = 20 \text{ m s}^{-1}$ shallow-shear simulation

The flow field at 2 km AGL for the $U_s = 20 \text{ m s}^{-1}$ shallow shear simulation (Figs. 3d,e,f) consolidates from a series of smaller-scale cyclonic and anticyclonic vortices along and just behind the leading edge of the line at 3 h, to dominant cyclonic and anticyclonic vortices just behind the southern and northern ends of the line, respectively, by 4.5 h. At 4 h (Fig. 11), the horizontal cross section of the flow field and θ_e at 2 km depicts the southern, cyclonic vortex in a horizontal gradient of θ_e , located just behind the southern end of the line. The vertical cross section through the centerline of the system (Fig. 12a) depicts stronger and deeper ascent at the leading edge of the system relative to the weaker shear case, with the rear-inflow jet remaining more elevated to near the leading edge of the system. Likewise, the zone of negative horizontal vorticity generated within the cold pool-updraft interface also extends to higher levels than for the weaker shear case, with, additionally, a region of significant positive horizontal vorticity now located near the surface beneath the elevated rear-inflow jet. A cross section of the buoyancy field through the centerline (Fig. 13) similarly reveals a deeper, stronger cold pool than for the weaker-shear simulation, with stronger positive buoyancy anomalies also evident aloft within the ascending front-to-rear flow. The deeper leading-line lifting and more elevated rear-inflow jet for this case is a result of a more optimal balance between the cold pool and stronger ambient vertical wind shear, as described by Weisman (1992). A vertical cross section taken south of the line-end vortex again depicts a much shallower circulation characterized by flow over the shallow cold pool (Fig. 12b).

As in the $U_s = 10 \text{ m s}^{-1}$ simulation, most of the vortex lines for this case loop upward, southward, and

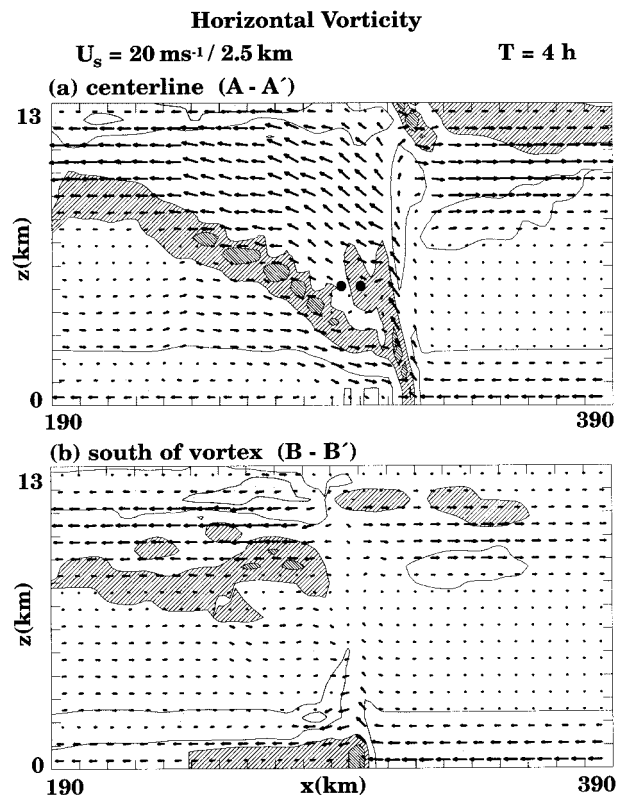


FIG. 12. East-west vertical cross sections of system-relative flow and horizontal vorticity for the $U_s = 20 \text{ m s}^{-1}$ simulations at 4 h, located (a) through the centerline of the system (A-A'), and (b) south of the line-end vortex (B-B'), as located on Fig. 11, as described for Fig. 7. A domain speed of $u_m = 18.5 \text{ m s}^{-1}$ has been subtracted from the flow field.

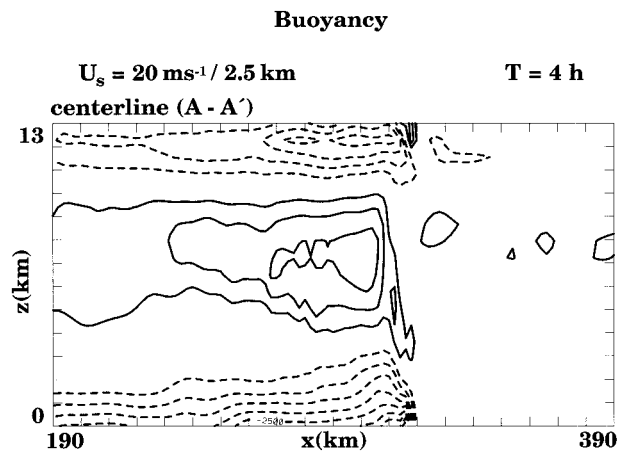


FIG. 13. East-west vertical cross sections of buoyancy for the $U_s = 20 \text{ m s}^{-1}$ simulations at 4 h, located through the centerline of the system (A-A'), as located on Fig. 11. The buoyancy field is contoured using a $500 \times 10^{-4} \text{ m s}^{-2}$ interval, with the zero contour omitted. Tick marks are spaced at 10-km intervals in the horizontal and 1-km intervals in the vertical.

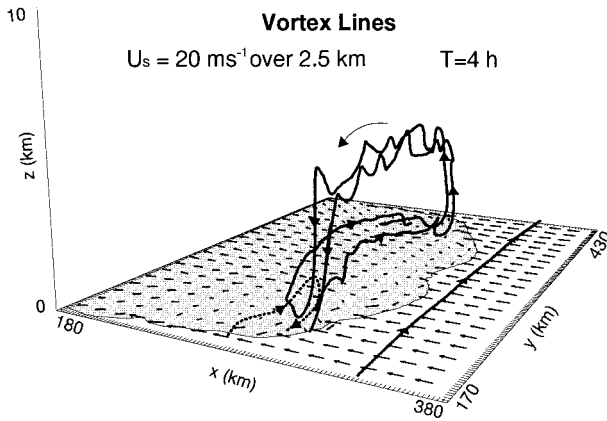


FIG. 14. Vortex-line structure at 4 h for the $U_s = 20 \text{ m s}^{-1}$ non-Coriolis simulation, as described for Fig. 9. The thick dashed line represents a vortex line that originates in the ambient shear layer ahead of the system.

downward through the line-end vortices. However, they now generally connect back northward at low levels to form nearly complete vortex loops (Fig. 14; the degree to which the vortex loops are not complete being due to interpolation errors). The southward-pointing vortex lines aloft are again associated with the system-generated negative horizontal vorticity, while the northward-pointing vortex lines at low levels are associated with the positive horizontal vorticity layer located beneath the elevated rear-inflow jet. The source of this positive horizontal vorticity is a combination of the ambient horizontal vorticity (e.g., that which is associated with the ambient shear layer) and the positive horizontal vorticity that was generated along the backside (western side) of the spreading surface cold pool. A few of the vortex lines emanating from the line-end vortex now also originate in the ambient shear layer ahead of the system (as represented by the dashed vortex line in Fig. 14), such vortex lines having been first tilted up within the leading-line updraft and then downward into the line-end

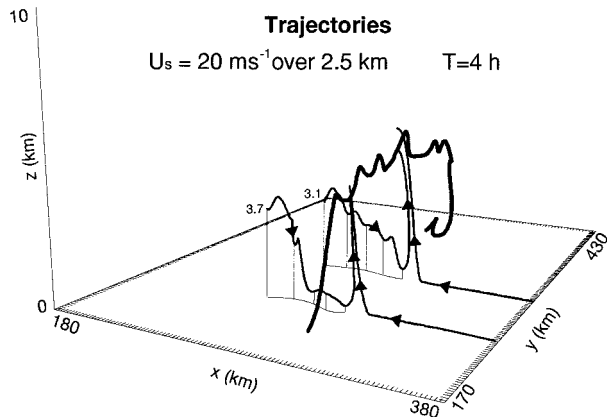


FIG. 15. Vortex-line and associated time-dependent trajectories at 4 h for the $U_s = 20 \text{ m s}^{-1}$ non-Coriolis simulation, as described for Fig. 10.

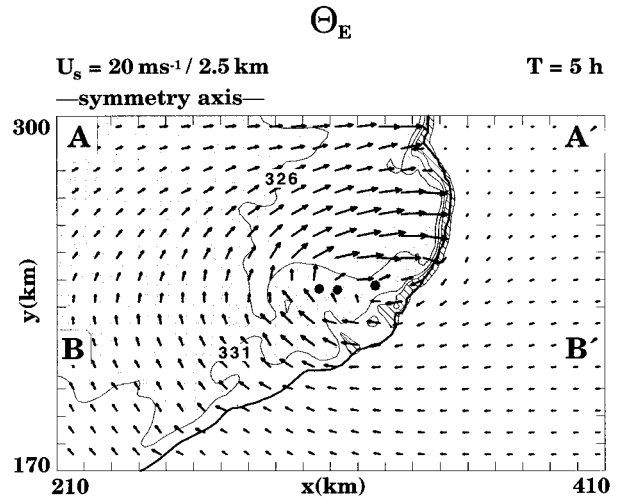


FIG. 16. Horizontal cross section of system-relative flow and θ_e at 2 km AGL for the $U_s = 20 \text{ m s}^{-1}$ simulation at 5 h, as described for Fig. 6. A domain speed of $u_m = 18.5 \text{ m s}^{-1}$ has been subtracted from the flow field.

vortex. Trajectory analyses (Fig. 15) again confirm that the air parcels making up the primary vortex lines originate both from the front and rear of the system.

By 5 h, the anticyclonic line-end vortex has grown in size and strength, expanding rearward but still remaining connected to the leading edge of the system (Fig. 16). A vertical cross section through the centerline (not shown) depicts an even more vertically erect circulation than earlier, along with a deeper and stronger elevated rear-inflow jet. The zone of negative horizontal vorticity is also deeper and stronger at the leading edge above 1 km AGL, but is now replaced by positive horizontal vorticity near the surface beneath the elevated rear-inflow jet. The three-dimensional vortex line structure at 5 h (Fig. 17) reflects the expanded size of the line-end vortices, with the upward looping extending farther behind the leading edge of the system, but unlike

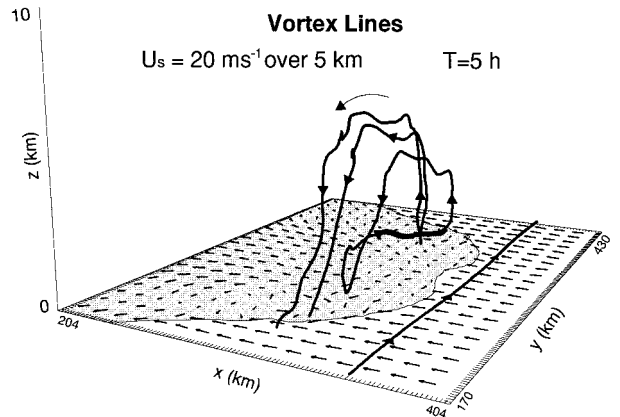


FIG. 17. Vortex-line structure at 5 h for the $U_s = 20 \text{ m s}^{-1}$ non-Coriolis simulation, as described for Fig. 9.

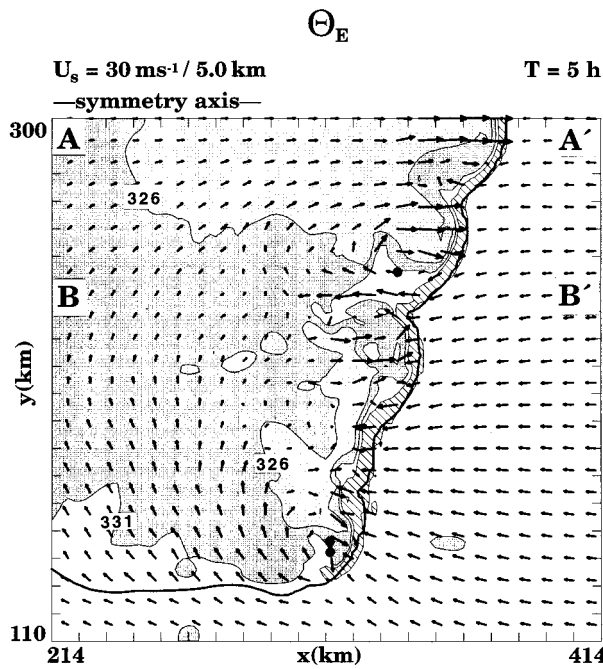


FIG. 18. Horizontal cross section of system-relative flow and θ_e at 2 km AGL for the $U_s = 30 \text{ m s}^{-1}$ simulation at 5 h, as described in Fig. 6. A domain speed of $u_m = 18.5 \text{ m s}^{-1}$ has been subtracted from the flow field.

at 4 h, no vortex lines could be identified as originating in the ambient shear layer.

c. The $U_s = 30 \text{ m s}^{-1}$ deeper-shear simulation

In contrast to the shallower-shear simulations, which are characterized by dominant system-scale line-end vortices after the initial 4 h, the $U_s = 30 \text{ m s}^{-1}$ deeper-shear case maintains a series of strong, subsystem-scale line-end vortices extending all along the line throughout the 6 h. At 5 h, the system at 2 km AGL is characterized by series of bow-shaped segments, each associated with its own pair of line-end vortices (Fig. 18). A vertical cross section through the centerline (Fig. 19a) of the system depicts a strong and deep leading-line convective updraft, with an elevated rear-inflow jet behind, similar to but deeper than in the $U_s = 20 \text{ m s}^{-1}$ shallow-shear case. The zone of negative horizontal vorticity also extends up higher than in the shallower-shear cases. A vertical cross section taken south of one of the subsystem-scale vortices (Fig. 19b) again shows a much shallower circulation at the leading edge of the system, characterized by flow over a shallower cold pool.

With the many strong, deep cells and related subsystem-scale vortices along the line, the vortex lines do not reveal as coherent a system-scale structure as in the shallow-shear cases. Still, two primary types of vortex-line configurations can be identified at 5 h (Fig. 20). The first type is as described for the shallow-shear cases, consisting of vortex lines that tilt up, southward, and

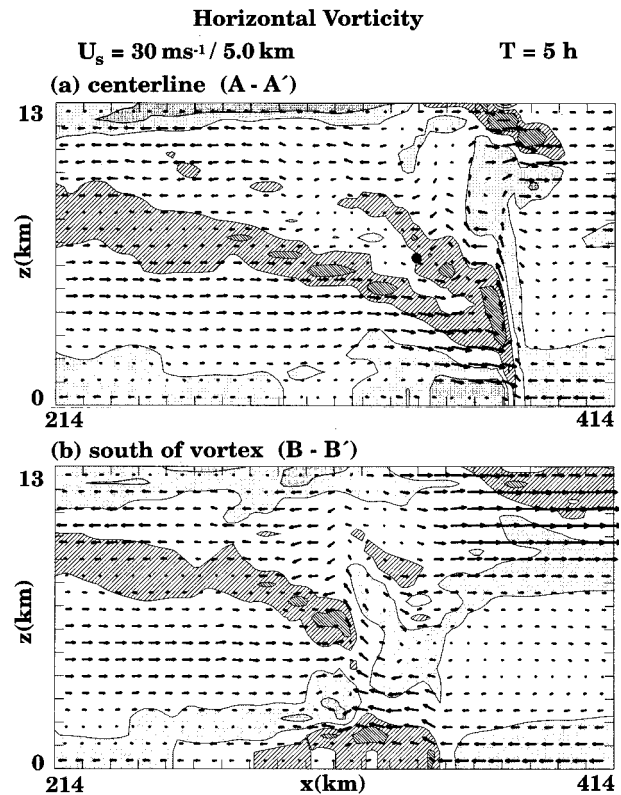


FIG. 19. East-west vertical cross sections of system-relative flow and horizontal vorticity for the $U_s = 30 \text{ m s}^{-1}$ simulations at 5 h, located (a) through the centerline of the system (A-A'), and (b) south of the line-end vortex (B-B'), as located in Fig. 18, as described for Fig. 7. A domain speed of $u_m = 18.5 \text{ m s}^{-1}$ has been subtracted from the flow field.

then down through line-end vortex pairs associated with subsystem-scale convective line segments. This configuration is shown for the double bow-shaped segment centered on the symmetry axis at this time. Such a configuration of vortex lines is consistent with the source of the vorticity being the tilting of the system generated negative horizontal vorticity, as previously discussed.

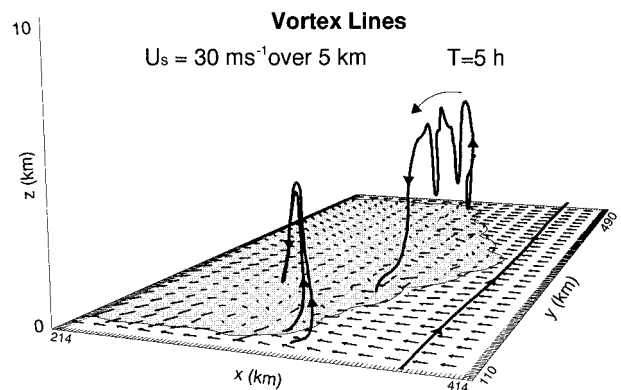


FIG. 20. Vortex-line structure at 5 h for the $U_s = 30 \text{ m s}^{-1}$ non-Coriolis simulation, as described for Fig. 9.

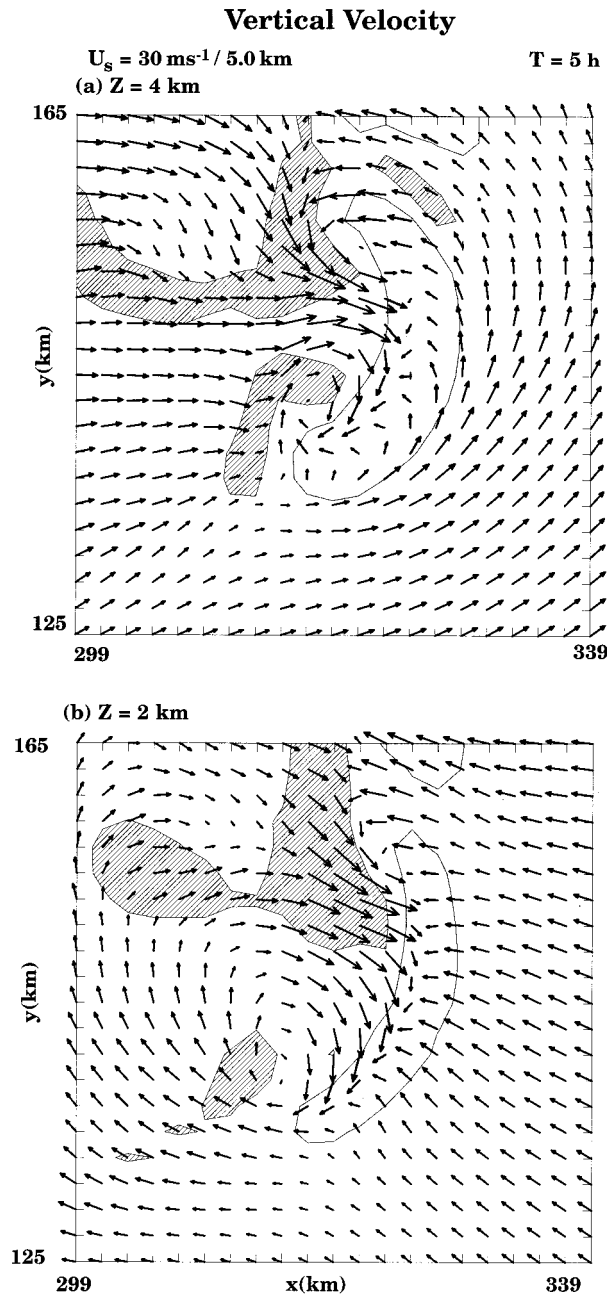


FIG. 21. Horizontal cross section of storm-relative winds and vertical velocity (shaded for greater than 5 m s^{-1} and cross hatched for less than -2 m s^{-1}) at (a) 4 km and (b) 2 km AGL for the southernmost cell for the $U_s = 30 \text{ m s}^{-1}$ simulation at 5 h. A domain speed of $u_m = 18.5 \text{ m s}^{-1}$ has been subtracted from the flow field. Tick marks are spaced at 10-km intervals.

The second type of vortex line originates in the ambient shear layer ahead of the system, is tilted upward within the leading line updraft and then back downward within the line-end vortex. A good example of this configuration is the anticyclonic vortex located at the southern end of the system at this time. Horizontal cross sections at 2 km and 4 km AGL centered on this vortex

(Fig. 21) shows that this vortex-line configuration is associated with a cyclonic updraft–anticyclonic down-draft vortex couplet associated with the southernmost cell within this system. This configuration is characteristic of supercell storms (e.g., Klemp 1987), suggesting that supercell dynamics may also be playing a role in the formation of these line-end vortices for such stronger, deeper-shear cases. A similar configuration of vortex lines was noted by Weisman (1993) during the early stages in the evolution of book-end vortices associated with severe bow echoes. The bow echoes in that study evolved in environments with 2.5 km AGL shears of $U_s = 25 \text{ m s}^{-1}$ or greater, with the line-end cells again being characterized as supercellular at early times, having originated via a splitting process.

5. Mechanisms of vortex formation: Vorticity equation analysis

The source for the system-scale line-end vortices can be clarified further through the use of the flux form of the vertical vorticity equation, that is,

$$\frac{\partial \zeta}{\partial t} = -\frac{\partial}{\partial x} \left[w \frac{\partial v}{\partial z} + u(f + \zeta) \right] - \frac{\partial}{\partial y} \left[-w \frac{\partial u}{\partial z} + v(f + \zeta) \right]. \tag{4}$$

By applying the divergence theorem, one can use (4) to formulate an equation for the circulation, which has the following form when applied to a box of area A that extends from the center of the system to far outside the northern (or southern) extent of the line-end vortex and a long distance east and west of the active convection (Fig. 22),

$$\begin{aligned} \frac{\partial C}{\partial t} &= \iint_A \frac{\partial \zeta}{\partial t} \\ &= \oint f \mathbf{v} \cdot \mathbf{n} \, dl + \int_a^b \left[-w \frac{\partial u}{\partial z} + v \zeta \right] dx, \end{aligned} \tag{5}$$

where \mathbf{n} is the unit vector normal to the prescribed circuit, and where a and b define a line along the symmetry axis of the system. It is assumed that the vertical velocity and relative vorticity are negligible far from the convective zone. The terms contributing to the rate of change of circulation over the prescribed box thus simplify down to the flux of Coriolis rotation into or out of the box, and a line integral through the center of the convective system that includes contributions from the vertical flux of horizontal vorticity (westerly or easterly shear) as well as the north–south flux of relative vorticity through that boundary of the box.

For a case with non-Coriolis forcing and with north–south symmetry (as is the case for the purely westerly-shear simulations), this expression simplifies further to

$$\frac{\partial C}{\partial t} = \int_a^b \left[-w \frac{\partial u}{\partial z} \right] dx \equiv \int_a^b F_w \, dx, \tag{6}$$

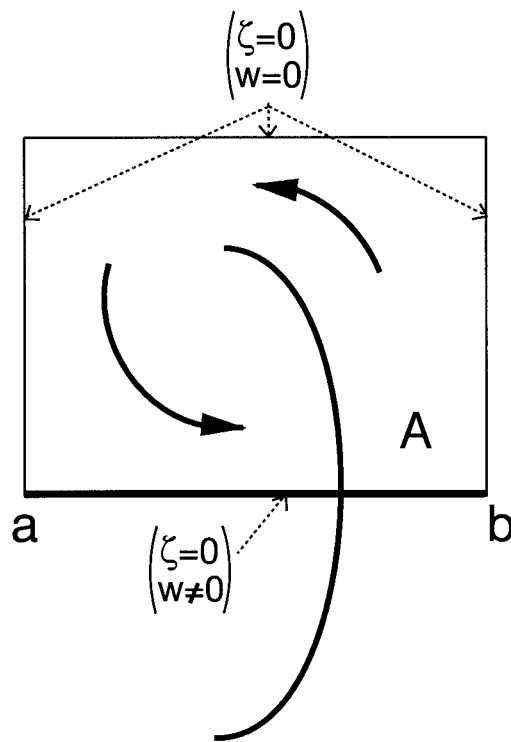


FIG. 22. Schematic of circulation analysis.

which shows that the source for the system-scale line-end vortices in the symmetric simulations must ultimately be traced to the net vertical flux of horizontal vorticity (embodied in the westerly or easterly shear) along the centerline of the system. This again shows that a cyclonic northern line-end vortex could result from either a localized downdraft in westerly shear or a localized updraft in easterly shear, as schematically described in Fig. 5 using vortex lines. A mirror-image circulation analysis likewise results in the production of an anticyclonic southern line-end vortex.

In order to further elucidate the source of circulation for the present simulations, east–west vertical cross sections of F_w through the center of each convective system are presented for the $U_s = 10, 20,$ and 30 m s^{-1} non-Coriolis shear cases at 4.0 h in Fig. 23. This time was found to be representative of the growth period of the vortices, as evident from Figs. 3 and 4. For the present purposes, the vorticity forcing terms are averaged over a 40-km wide area to emphasize more of the system-scale aspects of the line-end vortex forcing. Averaged system-relative vectors are also included on each figure to discern the system-scale flow field.

For all three shear cases, F_w is positive and concentrated in a relatively narrow zone near the leading edge of the convective line. Net positive forcing along the centerline of the system results in the generation of net positive circulation within the box centered around the northern end of the convective system as well as net negative circulation within a box centered around the

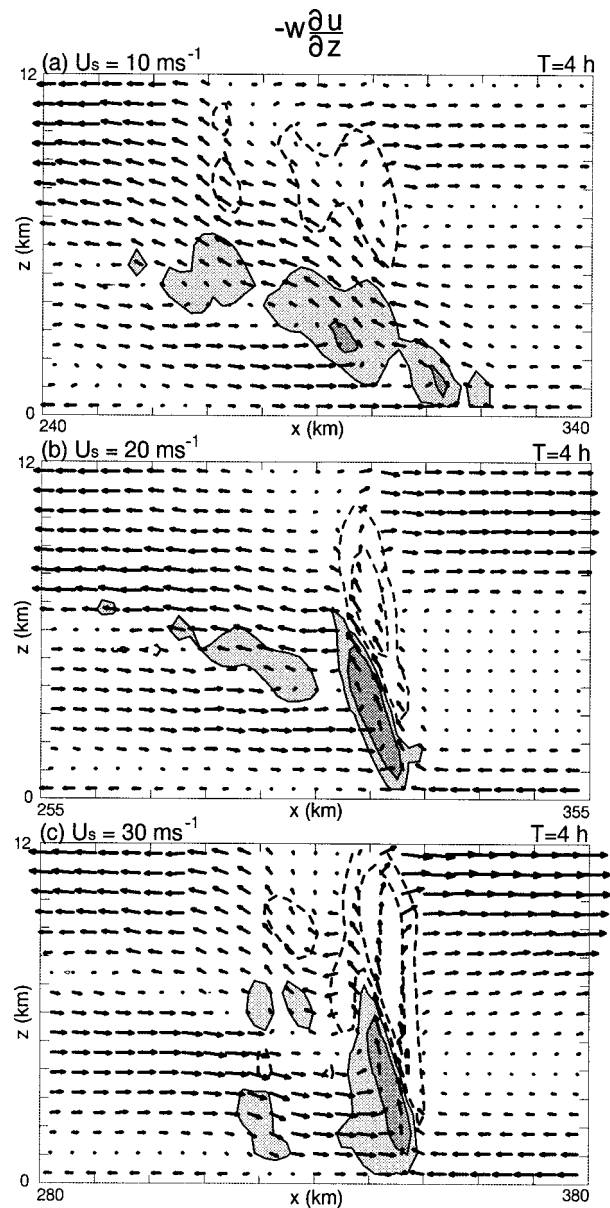


FIG. 23. Averaged east–west vertical cross section of system-relative flow and F_w for (a) $U_s = 10 \text{ m s}^{-1}$, (b) $U_s = 20 \text{ m s}^{-1}$, and (c) $U_s = 30 \text{ m s}^{-1}$ simulations at 4 h. Fields are averaged over a 40-km north–south region centered on the symmetry axis, and contoured for values $> 0.03 \text{ m s}^{-2}$ (darkly shaded), $> 0.0075 \text{ m s}^{-2}$ (lightly shaded), -0.0075 m s^{-2} , and -0.03 m s^{-2} , with both negative contours dashed. A domain speed of $u_m = 13.0, 18.5,$ and 18.5 m s^{-1} has been subtracted from the flow field for the $U_s = 10, 20,$ and 30 m s^{-1} shear cases, respectively. Tick marks are spaced at 10-km intervals in the horizontal and 1-km intervals in the vertical.

southern end of the system, which is consistent with the observed pattern of positive and negative line-end vortices. This positive forcing is associated with a front-to-rear ascending current superposed on easterly vertically sheared horizontal flow, which is again consistent with the previous vortex-line analyses, which suggests

that it is localized lifting of the system-generated horizontal vorticity that produces the line-end vortices. For the $U_s = 10 \text{ m s}^{-1}$ weak-shear case, the forcing is tilted strongly westward, spreading significantly rearward of the leading edge of the system, which is consistent with the line-end vortices also extending significantly behind the active convection. For the stronger-shear $U_s = 20$ and 30 m s^{-1} cases, the forcing is more erect, and both sets of line-end vortices are restricted to just behind the leading edge of the system.

The mechanisms for the generation of the system-scale line-end vortices can also be revealed by averaging (4) in the cross-line direction, again assuming that the relative vorticity and vertical velocity are close to zero at far distances east and west of the active convective zone, that is,

$$\frac{\partial \bar{\zeta}}{\partial t} = -\frac{\partial}{\partial y}[-\overline{F_w} + \overline{v(f + \zeta)}] - uf|_a^b, \quad (7)$$

where

$$\overline{(\quad)} = -\frac{1}{L} \int_a^b dx, \quad (8)$$

where L is the averaging distance. In the absence of Coriolis forcing and relative vorticity initially, this expression shows that local rates of change of across-line-averaged vertical vorticity are forced by north–south variations in F_w .

Across-line-averaged cross sections of F_w for the $U_s = 10, 20,$ and 30 m s^{-1} non-Coriolis shear cases at 4 h are presented in Fig. 24. For this purpose, F_w has been smoothed using a 20-point running mean filter to emphasize more of the system-scale features. All three shear cases depict a pattern of positive F_w within the lowest several kilometers AGL within the active convective zone, with negative contributions above. From a system-scale perspective, the limited north–south extent of the positive F_w is what leads to the systematic development of the line-end vortices, with the mean negative gradient evident on the northern end of the system leading to the development of a cyclonic vortex, and the mean positive gradient on the southern end of the system leading to the development of the anticyclonic vortex. Likewise, opposite sign line-end vortices would be expected to develop aloft. Such vortices are indeed observed in the present simulations (not shown), but are much weaker than the lower-level vortices (e.g., Skamarock et al. 1994a).

The above analysis can equally be applied to divulge the source for the subsystem-scale line-end vortices, since there would also be a tendency to produce cyclonic and anticyclonic pairs of vortices associated with any localized maximum (or minimum) in F_w along the line (assuming the same north–south symmetry evident with the system-scale features). The association between the tendency to produce subsystem vortices and the along-line structure in F_w is evident in comparing the hori-

zontal cross sections of F_w at 2 km AGL for the $U_s = 20$ and 30 m s^{-1} simulations. For the $U_s = 20 \text{ m s}^{-1}$ case at 4 h (Fig. 25), there is very little structure in F_w along the line, and only system-scale line-end vortices are evident. For the $U_s = 30 \text{ m s}^{-1}$ case at 4 h (Fig. 26a), there are several bow-shaped maxima of F_w along the line, with each maximum associated with its own pair of line-end vortices. The F_w forcing has consolidated into fewer bow-shaped segments by 5 h (Fig. 26b), but each segment is still associated with its own set of line-end vortices.

The fact that distinct maxima are more evident in the deeper shear case seems most related to the tendency to maintain stronger, cellular-scale structures along the line. For the shallower-shear simulations, the initially imposed line of cells is overwhelmed by the circulation generated by a strong, system-scale cold pool by 4 h, resulting in a predominantly two-dimensional updraft structure between the line ends. For the $U_s = 30 \text{ m s}^{-1}$ deeper shear case, the cold pool generated by stronger convective cells has been able to overcome the ambient shear locally by 4 h, leading to the development of smaller bow-shaped segments along the line, but it has yet to consolidate on a system-scale, allowing strong, three-dimensional cellular entities, such as supercells, to continue to survive. The system-scale cold pool has become more uniform by 5 h, though, resulting in larger bow-shaped segments and a gradual enhancement of the system-scale line-end vortices. Cellular-scale features are now confined nearer the ends of the system, where the cells are more free to interact with the ambient shear to develop three-dimensional features. The system-scale cold pool continues to strengthen and consolidate over time (e.g., Fig. 3i), and one would expect that eventually, the subsystem-scale vortices along the line would disappear completely, in favor of the more system-scale line-end vortices, as was also noted for the $U_s = 20 \text{ m s}^{-1}$ shear case.

The difference in forcing characteristics for the vortices generated by the tilting of system-generated horizontal vorticity and the tilting of the ambient shear are highlighted further in Fig. 26b. We recall from section 4c that the anticyclonic vortex at the southern end of the line at this time was part of a cyclonic–anticyclonic updraft–downdraft supercellular couplet, with the vortex lines originating in the ambient shear layer ahead of the system (e.g., Figs. 20, 21). Consistent with this, there is much less positive F_w forcing associated with this vortex, as compared to the bow-shaped segments to the north. Instead, we see some signs of a weak negative–positive couplet of F_w forcing on the southeast flank of the vortex, as would be more consistent with an updraft–downdraft couplet acting on the ambient shear layer. It is likely that such ambient shear-produced vortices for strong, deep-shear cases play a critical role in maintaining a more broken, three-dimensional character to the line, especially at early times. This more broken-line structure then more readily promotes the

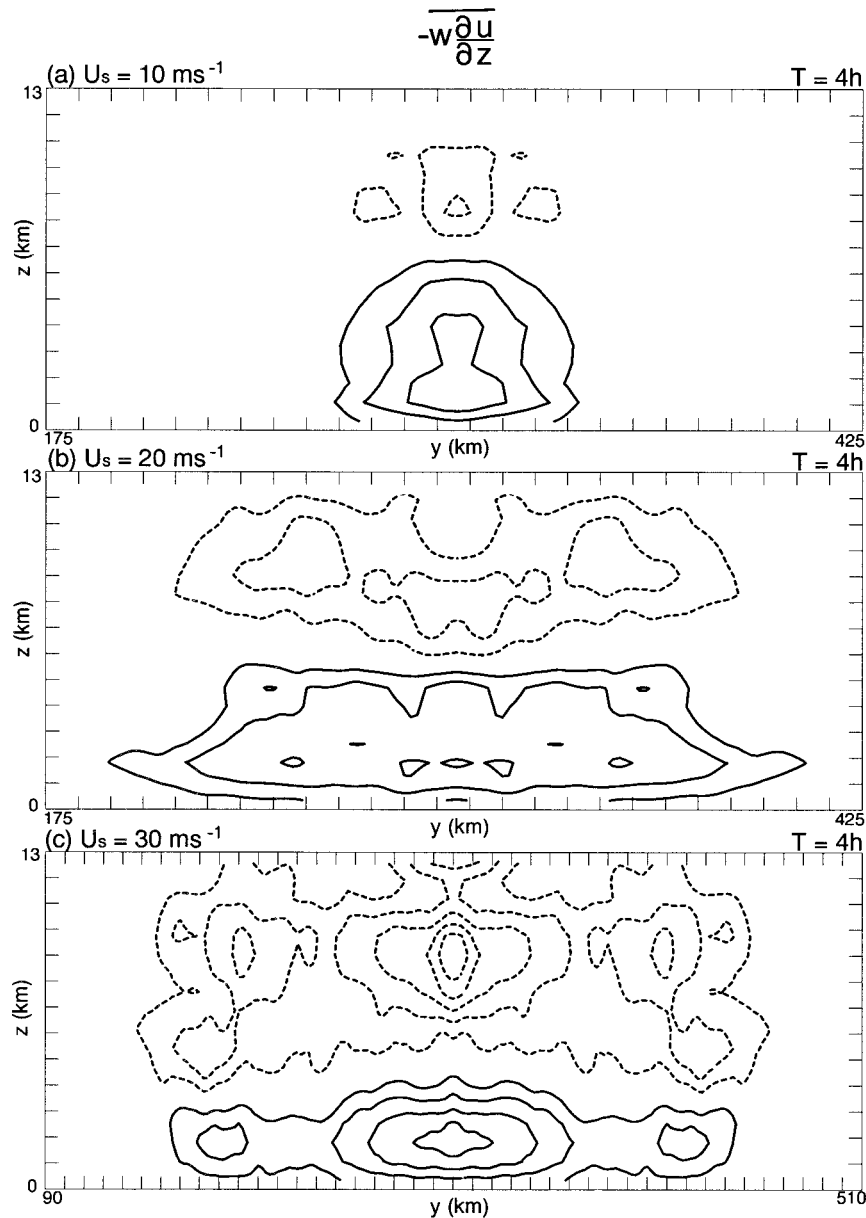


FIG. 24. Averaged north-south vertical cross section of smoothed F_w for (a) $U_s = 10 \text{ m s}^{-1}$, (b) $U_s = 20 \text{ m s}^{-1}$, and (c) $U_s = 30 \text{ m s}^{-1}$ simulations at 4 h. Fields are averaged over the entire domain in the east-west direction. The F_w is smoothed using a 20-point running mean filter in the horizontal, and contoured using a 0.0004 m s^{-2} interval, with the zero contour omitted. Tick marks are spaced at 10-km intervals in the horizontal and 1-km intervals in the vertical.

development of the subsystem-scale F_w -forced line-end vortices, which further promotes the development of the subsystem scale bow-shaped structures.

6. Coriolis influences

While the analysis in this paper has concentrated on diagnosing the source of the line-end vortices for the non-Coriolis simulations, the results from the Coriolis simulations (Fig. 4) demonstrate that Coriolis effects

can significantly affect system evolution after 4.5 h. As described previously by Skamarock et al. (1994a) for a weaker-shear simulation ($U_s = 10 \text{ m s}^{-1}$ over 2.5 km), the primary role of the Coriolis force is to promote the development of the cyclonic versus anticyclonic system-scale line-end vortex, due to midlevel convergence of Coriolis rotation [as is evident from both Eqs. (2) and (4)]. Much of this midlevel convergence is associated with the development of the rear-inflow jet, although the flow within the front-to-rear ascending current also

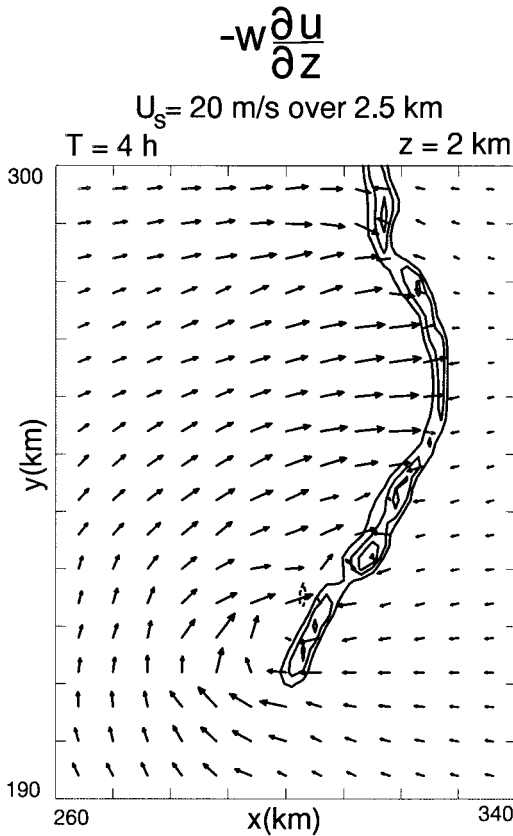


FIG. 25. Horizontal cross section of F_w at 2 km AGL for the $U_s = 20 \text{ m s}^{-1}$ simulation at 4 h. The F_w is contoured using a 0.03 m s^{-2} interval, with the zero contour omitted. Storm-relative wind vectors are presented every third grid point (6 km), with a vector length of one grid point equal to a wind magnitude of 7.5 m s^{-1} . A domain speed of $u_m = 18.5 \text{ m s}^{-1}$ has been subtracted from the flow field. Tick marks are spaced at 10-km intervals.

contributes somewhat to the net convergence. This effect of the Coriolis forcing was used to explain the common observation of system-scale evolution to an asymmetric structure, as described in the introduction.

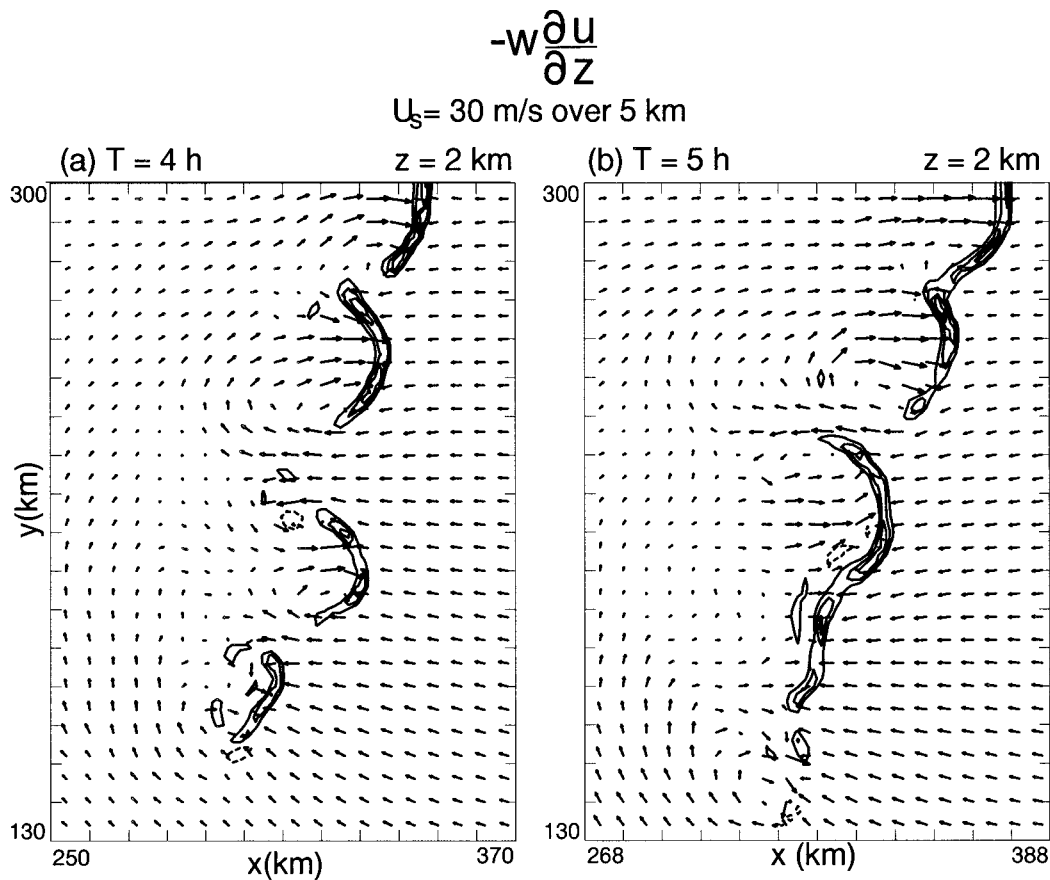
The present results emphasize that this effect also operates for stronger-shear cases as well, and, in addition, operates on both the system and subsystem scale. The effects on subsystem-scale vortices are especially evident in the $U_s = 30 \text{ m s}^{-1}$ shear Coriolis simulation between 4.5 and 6 h, where we observe the evolution of the southernmost bow-shaped segment from a symmetric to asymmetric structure over this time period (Figs. 4h,i). A similar evolution is also noted for a smaller bow-shaped segment just to its north. On the other hand, there is less evidence of system-scale cyclonic circulation developing for the $U_s = 30 \text{ m s}^{-1}$ case than for the $U_s = 10$ or 20 m s^{-1} simulations. This is due to the slower evolution of a system-scale rear-inflow jet for the $U_s = 30 \text{ m s}^{-1}$ case, as the strong, deeper ambient shear maintains a more vertically erect leading-line circulation than in the shallower and weaker shear cases.

As described by Weisman (1992), rear-inflow jets are generated in response to the upshear tilting of the leading-line convective circulation, as the cold-pool-generated circulation overwhelms the ambient shear. For the $U_s = 10$ and 20 m s^{-1} shallow-shear cases, the cold-pool circulation has overwhelmed the ambient shear system wide by 4 h, and a system-scale rear-inflow jet has become well established. However, for the $U_s = 30 \text{ m s}^{-1}$ case, the cold-pool circulation has overwhelmed the ambient shear only locally by 4 h, and a system-scale rear-inflow jet and the associated cyclonic circulation is much slower to develop.

7. Summary and discussion

The results presented herein point to two sources for the system-scale and subsystem-scale vortices produced in the idealized non-Coriolis simulations. The primary source appears to be the tilting of system-generated horizontal vorticity within the laterally finite front-to-rear ascending current. This process systematically produces a cyclonic vortex behind the northern end of the system and an anticyclonic vortex behind the southern end of the system. The ambient shear plays an important role in this process by producing a preferred zone of lifting along the downshear edge of the system, due to cold-pool shear interactions, thus, effectively limiting the lateral extent of the lifting zone. For weak shear, a shallow front-to-rear ascending current leads to vortex production well behind the leading edge of the system, while for stronger shears, a stronger, more vertically erect leading-line updraft results in vortices forming just behind the leading edge of the system. An analysis using the flux form of the vertical vorticity equation further elucidates this vortex formation mechanism as the natural consequence of localized lifting within easterly shear, the easterly shear in this case being generated by the horizontal buoyancy gradients between the system-scale updraft and downdraft (cold pool).

For all the shear cases presented, significant line-end vortex generation by this mechanism does not commence until after 3 h into the simulation, which is a minimum time it takes to generate a well-organized ascending front-to-rear and descending rear-inflow current. Consistent with this, system-scale line-end vortex formation is further delayed in the stronger-shear cases, as it takes longer for the cold-pool-generated circulation to overwhelm the ambient shear. Additional simulations (not shown) also suggest that the timescale for vortex generation decreases for a decreasing initial length of the convective system. This may be due to the positive feedback that can occur if the vortices are close enough such that their flow fields can reinforce each other. An enhanced, elevated rear-inflow jet between the vortices can lead to enhanced lifting at the leading edge of the system (e.g., Weisman 1992), which can lead to enhanced tilting of system-generated horizontal vorticity at the ends of the system, etc. Such a feedback was



at the system ends, cyclonic to the south and anticyclonic to the north (for westerly ambient shear). The convectively generated cold pool must also be represented properly so that the cold-pool-generated horizontal vorticity can be tilted to produce the proper line-end vortex structure.

One of the important questions that is not addressed sufficiently by this study is how the scale of the system- and subsystem-scale vortices is determined. Since such vortices form readily in the absence of Coriolis forcing, there is no obvious dynamical scale, such as a Rossby radius of deformation, to point to ultimately control the systems' scale. One could argue that the scale of the system-scale vortices is simply controlled by the length of the initial convective line. However, Skamarock et al. (1994a) found that, for a given ambient shear, the final scale of the convective system was largely independent of initial line length. From these results, it appears that the final scale chosen for the system tends to increase for increasing ambient shear strength and depth. This seems to make sense, in that the stronger, deeper shear cases produce a more favorable balance with the convectively generated cold pools (Rotunno et al. 1988), leading to an expanding region of convective triggering as the cold pool grows in size. On the other hand, the $U_s = 20 \text{ m s}^{-1}$ shallow-shear case first grows in scale, but then shrinks again as the line-end vortices strengthen, suggesting that the vortices are also influencing the resultant system scale. The subsystem vortices originate over a range of scales, but the smaller systems tend to congeal over time to perhaps a preferred scale in the 40–80-km range. One possibility is that the scale is chosen somewhat based on the ability of the vortices along the line to interact favorably with each other, by strengthening the resulting rear-inflow jet, which affects the lifting at the leading edge of the system, etc., as discussed in Weisman (1993) for more isolated bow echoes. Any further resolution of these issues, however, must await further study.

Acknowledgments. We would like to gratefully acknowledge valuable discussions and reviews of this manuscript by William C. Skamarock, Rajul E. Pandya, Stanley B. Trier, and the anonymous reviewers.

REFERENCES

- Bartels, D. L., and R. A. Maddox, 1991: Midlevel cyclonic vortices generated by mesoscale convective systems. *Mon. Wea. Rev.*, **119**, 104–118.
- Brandes, E. A., 1990: Evolution and structure of the 6–7 May 1985 mesoscale convective system and associated vortex. *Mon. Wea. Rev.*, **118**, 109–127.
- Burgess, D. W., and B. F. Smull, 1990: Doppler radar observations of a bow echo associated with a long-track severe windstorm. Preprints, *16th Conf. on Severe Local Storms*, Kananaskis Park, AB, Canada, Amer. Meteor. Soc., 203–208.
- Davis, C. A., and M. L. Weisman, 1994: Balanced dynamics of mesoscale vortices produced in simulated convective systems. *J. Atmos. Sci.*, **51**, 2005–2030.
- Fritsch, J. M., J. D. Murphy, and J. S. Kain, 1994: Warm core vortex amplification over land. *J. Atmos. Sci.*, **51**, 1780–1807.
- Fujita, T. T., 1978: Manual of downburst identification for Project Nimrod. Satellite and Mesometeorology Research Paper 156, Dept. of Geophysical Sciences, University of Chicago, Chicago, IL, 104 pp.
- Houze, R. A., S. A. Rutledge, M. I. Biggerstaff, and B. F. Smull, 1989: Interpretation of Doppler weather radar displays of mid-latitude mesoscale convective systems. *Bull. Amer. Meteor. Soc.*, **70**, 608–619.
- , B. F. Smull, and P. Dodge, 1990: Mesoscale organization of springtime rainstorms in Oklahoma. *Mon. Wea. Rev.*, **118**, 613–654.
- Johns, R. H., and W. D. Hirt, 1987: Derechos: Widespread convectively induced windstorms. *Wea. Forecasting*, **2**, 32–49.
- Jorgensen, D. P., M. A. LeMone, and S. B. Trier, 1997: Structure and evolution of the 22 February 1993 TOGA COARE squall line: Observations of precipitation, circulation, and surface energy fluxes. *J. Atmos. Sci.*, **54**, 1961–1985.
- Klemp, J. B., 1987: Dynamics of tornadic thunderstorms. *Annu. Rev. Fluid Mech.*, **19**, 369–402.
- , and R. B. Wilhelmson, 1978: The simulation of three-dimensional convective storm dynamics. *J. Atmos. Sci.*, **35**, 1070–1096.
- Loehrer, S. M., and R. H. Johnson, 1995: Surface pressure and precipitation life cycle characteristics of PRE-STORM mesoscale convective systems. *Mon. Wea. Rev.*, **123**, 600–621.
- Maddox, R. A., 1980: Mesoscale convective complexes. *Bull. Amer. Meteor. Soc.*, **61**, 1374–1387.
- Menard, R. D., and J. M. Fritsch, 1989: A mesoscale convective complex-generated inertially stable warm core vortex. *Mon. Wea. Rev.*, **117**, 1237–1260.
- Przybylinski, R. W., 1995: The bow echo: Observations, numerical simulations, and severe weather detection methods. *Wea. Forecasting*, **10**, 203–218.
- Rotunno, R., J. B. Klemp, and M. L. Weisman, 1988: A theory for strong, long-lived squall lines. *J. Atmos. Sci.*, **45**, 463–485.
- Schmidt, J. M., and W. R. Cotton, 1989: A high plains squall line associated with severe surface winds. *J. Atmos. Sci.*, **46**, 281–302.
- Scott, J. D., and S. A. Rutledge, 1995: Doppler radar observations of an asymmetric mesoscale convective system and associated vortex couplet. *Mon. Wea. Rev.*, **123**, 3437–3457.
- Skamarock, W. C., M. L. Weisman, and J. B. Klemp, 1994a: Three-dimensional evolution of simulated long-lived squall lines. *J. Atmos. Sci.*, **51**, 2563–2584.
- , —, C. A. Davis, and J. B. Klemp, 1994b: The evolution of simulated mesoscale convective systems in idealized environments. Preprints, *Sixth Conf. on Mesoscale Processes*, Portland, OR, Amer. Meteor. Soc., 407–410.
- Smull, B. F., and J. A. Augustine, 1993: Multiscale analysis of a mature mesoscale convective system. *Mon. Wea. Rev.*, **121**, 103–132.
- Stirling, J., and R. M. Wakimoto, 1989: Mesoscale vortices in the stratiform region of a decaying midlatitude squall line. *Mon. Wea. Rev.*, **117**, 452–458.
- Trier, S. B., and D. B. Parsons, 1995: Updraft dynamics within a numerically simulated subtropical rainband. *Mon. Wea. Rev.*, **123**, 39–58.
- , W. C. Skamarock, M. A. LeMone, and D. B. Parsons, 1996: Structure and evolution of the 22 February 1993 TOGA COARE squall line: Numerical simulations. *J. Atmos. Sci.*, **53**, 2861–2886.
- , —, and —, 1997: Structure and evolution of the 22 February 1993 TOGA COARE squall line: Organization mechanisms inferred from numerical simulation. *J. Atmos. Sci.*, **54**, 386–407.
- Weisman, M. L., 1992: The role of convectively generated rear-inflow jets in the evolution of long-lived mesoconvective systems. *J. Atmos. Sci.*, **49**, 1826–1847.
- , 1993: The genesis of severe, long-lived bow-echoes. *J. Atmos. Sci.*, **50**, 645–670.
- , J. B. Klemp, and R. Rotunno, 1988: Structure and evolution of numerically simulated squall lines. *J. Atmos. Sci.*, **45**, 1990–2013.